Radio Interferometric Studies of Cool Evolved Stellar Winds

A dissertation submitted to the University of Dublin
for the degree of Doctor of Philosophy

Eamon O'Gorman

Supervisor: Dr. Graham M. Harper

Trinity College Dublin, September 2013

School of Physics
University of Dublin
Trinity College

Declaration

I declare that this thesis has not been submitted as an exercise for a degree at this or any other university and it is entirely my own work.

I agree to deposit this thesis in the University's open access institutional repository or allow the library to do so on my behalf, subject to Irish Copyright Legislation and Trinity College Library conditions of use and acknowledgement.

Name: Your Name

Signature: ..... **Date:** .....

Summary

You should write a nice summary here...

A dedication if you wish...

Acknowledgements

Some sincere acknowledgements...

List of Publications

Refereed

1. **O'Gorman, E.**, Harper, G. M., Brown, A., Brown, A., Drake, S., and Richards, A. M. S.
   "Multi-wavelength Radio Continuum Emission Studies of Dust-free Red Giants"
   The Astronomical Journal, Accepted, (2013)

2. Richards, A. M. S., Davis, R. J., Decin, L., Etoka, S., Harper, G. M., Lim, J. J., Garrington, S. T., Gray, M. D., McDonald, I., **O'Gorman, E.**, Wittkowski, M.
   "e-MERLIN resolves Betelgeuse at wavelength 5 cm"
   Monthly Notices of the Royal Astronomical Society Letters, 432, L61 (2013)

3. **O'Gorman, E.**, Harper, G. M., Brown, J. M., Brown, A., Redfield, S., Richter, M. J., and Requena-Torres, M. A.
   "CARMA CO(J = 2 - 1) Observations of the Circumstellar Envelope of Betelgeuse"
   The Astronomical Journal, 144, 36 (2012)

4. Sada, P. V., Deming, D., Jennings, D. E., Jackson, B. K., Hamilton, C. M., Fraine, J., Peterson, S. W., Haase, F., Bays, K., Lunsford, A., and **O'Gorman, E.**
   "Extrasolar Planet Transits Observed at Kitt Peak National Observatory"
   Publications of the Astronomical Society of the Pacific, 124, 212 (2012)

5. Sada, P. V., Deming, D., Jackson, B. K., Jennings, D. E., Peterson, S. W., Haase, F., Bays, K., **O'Gorman, E.**, and Lundsford, A.
"Recent Transits of the Super-Earth Exoplanet GJ 1214b"
The Astrophysical Journal Letters, 720, L215 (2010)

Non-Refereed

1. **O'Gorman, E.**, & Harper, G. M.
"What is Heating Arcturus' Wind?",
Proceedings of the 16th Cambridge Workshop on Cool Stars, Stellar Systems and the Sun. Astronomical Society of the Pacific Conference Series, 448, 691 (2011)

Contents

List of Figures

List of Tables

1

Targets, Instrumentation, and Observations

Two unique data sets were analyzed as part of this thesis. The first data set was a millimeter interferometric multi-configuration study of Betelgeuse's circumstellar envelope at 1.3 mm. In the first half of this chapter we give a detailed introduction to Betelgeuse and discuss our current understanding of the star and its complex stellar atmosphere. We give a description of the millimeter interferometer CARMA, which we used to study its complex outflow region on a number of spatial scales and also describe our observations which spanned ~ 2.5 yr. The second data set consisted of a multi-wavelength centimeter study of two non-dusty red gaints, Arcturus and Aldebaran. In the second half of this chapter we give a detailed introduction to both of these stars, including a description of their stellar properties, and their existing atmospheric models which we test against our data in Chapter **??**. We give a short discription of the VLA, which was the centimeter interferometer we used to study these stars, and finally describe our VLA observations.

1.1 Betelgeuse

Betelgeuse (α Ori: M2 Iab) is one of a pair of nearest red supergiants ($d = 197 \pm 45$ pc, Harper *et al.* 2008), the other being Antares (α Sco: M1.5 Iab + B2.5 V) which has a distance of 170 ± 29 pc (van Leeuwen, 2007). Betelgeuse has a limb darkened angular diameter of 44.28 ± 0.15 mas (Haubois *et al.*, 2009) and subtends the largest angular diameter of any star in the northern sky apart from the Sun. It is by far the best studied red supergiant and has been observed with various techniques from the radio to the UV. According to Harper *et al.* (2001), Betelgeuse probably was a runaway star from the star-formation region Ori OB1 (see, e.g., Hoogerwerf *et al.*, 2000), and was a spectral type O9 V star while on the main sequence where it had a mass of $\sim 20\ M_{\odot}$. The evolutionary models of Meynet & Maeder (2003) suggest that its current mass is $18\ M_{\odot}$ which corresponds to a surface gravity of 0.5 cm s^{-2} (i.e., $2 \times 10^{-5} g_{\odot}$). Its mass loss is characterized by low velocity outflows ($10 - 17$ km s^{-1}) and a mass loss rate of $\sim 3 \times 10^{-6}\ M_{\odot}$ yr^{-1} (Harper *et al.*, 2001). Like most late-type evolved stars, Betelgeuse's terminal wind velocity v_{∞} is smaller than the surface escape speed $v_{\rm esc}$ (values given in Table 1.1). This means that most of the energy and momentum are deposited into its flow within the first few stellar radii.

Betelgeuse has a large rotation period of ~ 17 yr (Uitenbroek *et al.*, 1998), which implies that it is probably experiencing very limited action of a solar-like dynamo. This rotation period is in stark contrast to the equatorial solar rotation rate which is just 24.5 days. Its large radius ($\sim 950\ R_{\odot}$) means that any possible remanent of a strong main sequence magnetic field is likely negligible due to a large dilution factor. In comparison to Sun like stars, its large radius also means that it has a large photospheric scale height ($H_{\star} \sim 0.01\ R_{\star}$). The expected result of this is the presence of no more than a few giant and stable convection cells in the photosphere Schwarzschild (1975). Such features should enhance the detectability of the magnetic fields generated through a turbulent dynamo (Vögler & Schüssler, 2007). Bedecarrax *et al.* (2013) have recently monitored Betelgeuse over a three year period using high resolution spectropolarimetry, and find a longitudinal magnetic field strength which varies in values ranging from

Table 1.1: Physical Properties of α Ori.

Property	Value	Reference
HD Number	39801	...
Spectral Type	M2 Iab	Perryman *et al.* (1997)
Apparent Magnitude (V)	0.45 ± 0.4	Perryman *et al.* (1997)
RA (ICRS: ep=J2000)	$05^{\rm h}55^{\rm m}10.305^{\rm s}$	van Leeuwen (2007)
dec (ICRS: ep=J2000)	$+07°24'25.430''$	van Leeuwen (2007)
Proper motion-RA (mas yr^{-1})	27.54	van Leeuwen (2007)
Proper motion-dec (mas yr^{-1})	11.30	van Leeuwen (2007)
π (mas)	5.07 ± 1.1	Harper *et al.* (2008)
d (pc)	197 ± 45	Harper *et al.* (2008)
Main Sequence $M_\star$ ($M_\odot$)	~ 20	Meynet & Maeder (2003)
Main Sequence Spectral Type	O9 V	Harper *et al.* (2008)
Current $M_\star$ ($M_\odot$)	~ 18	Meynet & Maeder (2003)
$\theta_{\rm UD}$ (mas)	43.33 ± 0.04	Perrin *et al.* (2004)
$\theta_{\rm LD}$ (mas)	44.28 ± 0.15	Haubois *et al.* (2009)
$R_\star$ ($R_\odot$)	950	Harper *et al.* (2008)
$T_{\rm eff}$ (K)	3650	Levesque *et al.* (2005)
$\rm Log_{10}\, L_\star/L_\odot$	5.10 ± 0.22	Harper *et al.* (2008)
$\rm Log_{10}\, g_\star$ (cm s^{-2})	-0.3	Meynet & Maeder (2003)
Heliocentric $v_{\rm rad}$ (km s^{-1})	20.7 ± 0.4	Harper *et al.* (2008)
$v_{\rm esc}$ (km s^{-1})	85	...
v_∞ (km s^{-1})	10, 17	Bernat *et al.* (1979)
$T_{\rm wind}$ (K)	< 4000	Lim *et al.* (1998)
$\dot{M}_\star$ ($M_\odot$ yr^{-1})	3×10^{-6}	Harper *et al.* (2001)
Photospheric $H_\star$ ($R_\star$)	0.006	...
[Fe/H]	0.05 ± 0.14	Ramírez *et al.* (2000)
O/C	2.5	Lambert *et al.* (1984)
Rotational period (yr)	17	Uitenbroek *et al.* (1998)
$B_\star$ (G)	$-3 \rightarrow +2 \pm 0.5$	Bedecarrax *et al.* (2013)
Chromosphere Model	...	Harper *et al.* (2001)
Wind Model	...	Harper *et al.* (2001)
Outer CSE	...	Rodgers & Glassgold (1991)
^{12}C/^{13}C	6 ± 1	Harris & Lambert (1984)
^{16}O/^{17}O	525 ± 250	Harris & Lambert (1984)
^{16}O/^{18}O	700 ± 300	Harris & Lambert (1984)

-3 ± 0.5 G to $+2 \pm 0.5$ G with temporal changes in the field strength occurring over timescales as short as a few weeks.

Various studies have assumed that Betelgeuse has a warm ($T_e \sim 8000$ K) extended atmosphere where ionized hydrogen dominates the electron density (e.g., Hartmann & Avrett, 1984; Newell & Hjellming, 1982). In fact, high resolution UV photon scattering imaging with the HST partially resolved the *hot* chromosphere revealing $6000-8000$ K plasma extending to more than 2 $R_\star$ (Gilliland & Dupree, 1996). However, Lim *et al.* (1998) spatially resolved Betelgeuse with the 'old' VLA at 5 different wavelengths and showed that the mean electron temperature is actually much cooler, i.e., $T_e = 2000 - 4000$ K and extends out to several stellar radii as shown in Figure 1.1. In fact, the mid-IR [Fe II] line studies of Harper *et al.* (2009) suggest that the temperature of the bulk of the plasma where the chromosphere has its largest filling factor is < 2500 K. Therefore, it appears that the hot chromospheric plasma has a small filling factor and co-exists with the much more abundant cool plasma within several stellar radii. Harper *et al.* (2001) constructed a detailed physical model for the inner atmosphere of Betelgeuse which reproduces the radio fluxes of Lim *et al.* (1998) and consists of electron temperature and gas densities as a function of radius.

In comparison to other well studied red supergiants such as VY CMa, Betelgeuse has a modest mass loss rate, a high gas-to-dust mass ratio of $200 - 1700$, and low molecular abundances (Harper *et al.*, 2001). However, it is known to possess a molecular shell known as a MOLsphere above its photosphere (Tsuji, 2000), and recently Verhoelst *et al.* (2006) and Perrin *et al.* (2007) have used the VLTI to establish some of its properties. They find the MOLsphere to have a geometrical thin extent (~ 0.1 $R_\star$) with a temperature of ~ 1500 K at ~ 1.4 $R_\star$, and contains molecules such as H_2O, SiO, and Al_2O_3. Notably, they suggest that this molecular layer is where dust nucleation commences in support of a dust-driven wind scenario. However, the existence of Al_2O_3 is disputed by Kamiński *et al.* (2013) who argue that the absence of AlO (which is required to form Al_2O_3) in the photospheric spectrum is puzzling, and verification by independent studies is needed. In addition, Woitke (2006) finds that the average temperature between $1 - 3$ $R_\star$ is too high for silicates to form, and indeed recent studies suggest that silicates are not formed inside ~ 23 $R_\star$ (Skinner *et al.*, 1997; Tatebe *et al.*, 2007).

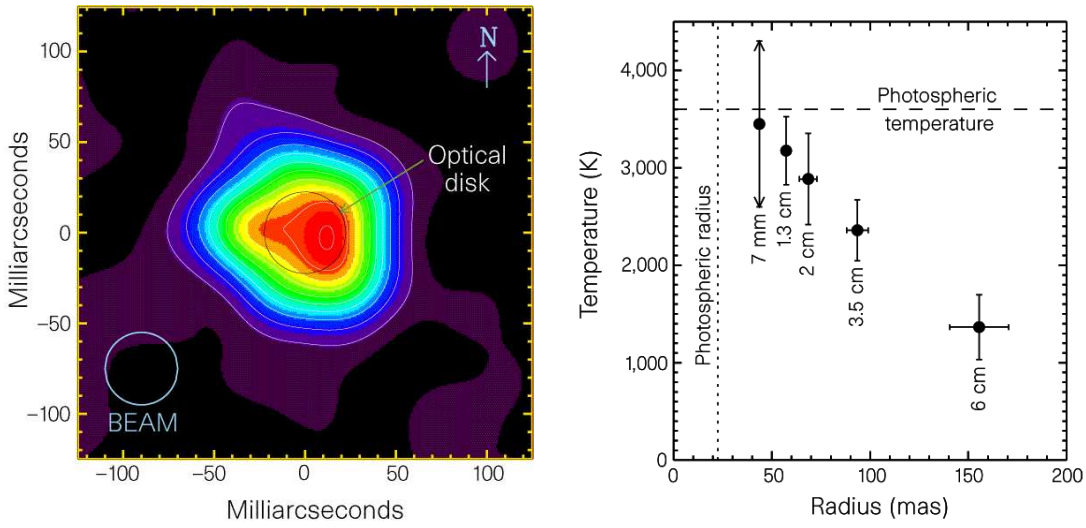

Figure 1.1: Left: The spatially resolved Q-band VLA image of Betelgeuse showing asymmetry in its atmosphere. Right: The multi-frequency spatially resolved radio maps revealed that the mean electron temperature profile was lower than expected (Lim *et al.*, 1998).

For Betelgeuse, it therefore appears that radiation pressure on dust grains is not the main mechanism driving its mass loss (Harper, 2010).

In the past decade or so, a number of sensitive multi-wavelength studies of Betelgeuse have revealed a complex non-spherically symmetric circumstellar environment. Starting at its surface, a H band interferometric image was reconstructed using data from the Infrared Optical Telescope Array (IOTA) and showed a non-uniform brightness distribution across its surface (Haubois *et al.*, 2009). This data was modelled with 3-D hydrodynamical simulations by Chiavassa *et al.* (2010), resulting in the detection of a granulation pattern on the surface. They concluded that the surface contains a large (~ 30 mas) convective cell and a few small to medium scale ($5 - 15$ mas) convection-related surface structures. Adaptive optics images with the Very Large Telescope (VLT) at $1.04 - 2.17\ \mu m$ revealed an irregular circumstellar envelope at a few $R_\star$ with a few bright plumes extending out to 6 $R_\star$ (Kervella *et al.*, 2009). These plumes have been attributed to the action of giant convection cells. Thermal infrared VLT ($\lambda = 8 - 20\ \mu m$) imaging revealed oxygen-rich dust out to 100 $R_\star$ ($2.5''$) (Kervella *et al.*, 2011), while Herschel images show a chaotic dust distribution far

out in the circumstellar envelope, i.e., beyond 600 $R_\star$ (i.e. $> 15''$) (Decin *et al.*, 2012). A conclusion that can be drawn from these studies is the constant presence of inhomogenities in the circumstellar environment which probably play a role in the formation of dust and molecular species. We defer a discussion on previous observations of CO in Betelgeuse's circumstellar environment until Chapter **??**.

1.2 CARMA

The Combined Array for Research in Millimeter-wave Astronomy (CARMA) (Bock, 2006) is a millimeter interferometer located at Cedar Flat in eastern California at an elevation of 2200 m. The array consists of nine 6.1 m antennas and six 10.4 m antennas formerly from the Berkeley Illinois Maryland Association (BIMA) and the Owens Valley Radio Observatory (OVRO) arrays respectively, and operates at 85-115 GHz (3 mm) and 215-270 GHz (1.3 mm). Eight additional 3.5 m antennas known as the Sunyaev-Zel'dovich Array (SZA) can also be added to CARMA for continuum observations at 26-36 GHz (1 cm) and 85-115 GHz (3 mm). The different sizes of the CARMA antennas makes it a heterogeneous array with a total collecting area equivalent to a single 32 m dish antenna. Despite some technical difficulties associated with image restoration for a heterogeneous array (e.g., the 15-element CARMA array has 3 different primary beams), there are a number of advantages. Such an array samples shorter $u-v$ spacings directly when the smallest antennas are in a compact configuration. This results in more of the total flux density being recovered and also recovers more of the large scale structure and is the reason why the smaller diameter antennas are usually left in the center of the array as shown in Figure 1.2. In fact, it has been shown that a heterogeneous CARMA array produces better image fidelity than a homogeneous array with the same number of antennas and collecting area (Wright, 1999).

CARMA is a reconfigurable array and has 5 different configurations providing baselines ranging between 8 m and 2 km; A configuration being the most extended and E configuration being the most compact. Figure 1.3 gives an overview of how these configurations are achieved at Cedar Flat. As the resolution is set by the array configuration and frequency of observation, we list the various achievable

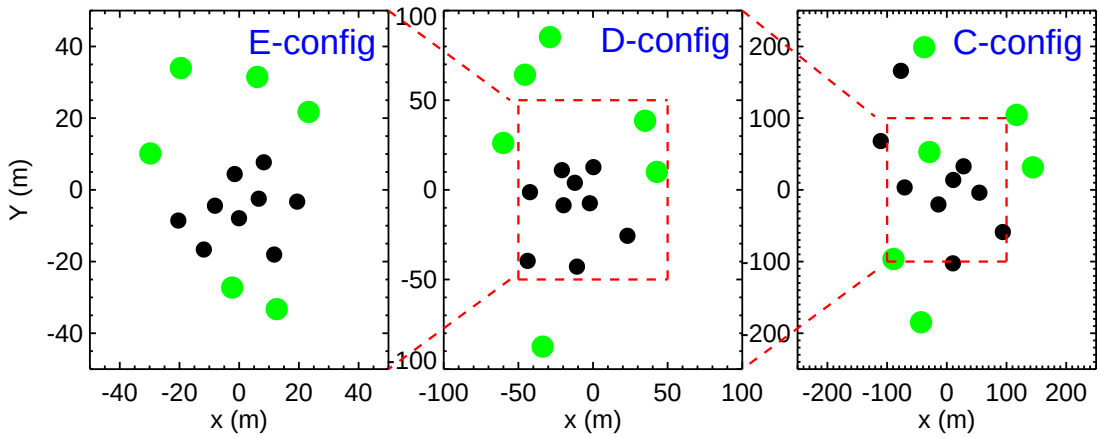

Figure 1.2: The three CARMA array configurations used to study to CSE of Betelgeuse. The most compact CARMA configuration is E configuration (*left*) which has $B_{\rm max}$ = 66 m, D configuration (*middle*) has $B_{\rm max}$ = 148 m, while C configuration (*right*) has $B_{\rm min}$ = 370 m and was the most extended configuration used in our study. The 10.4 m antennas are marked green while the 6.1 m antennas are marked black.

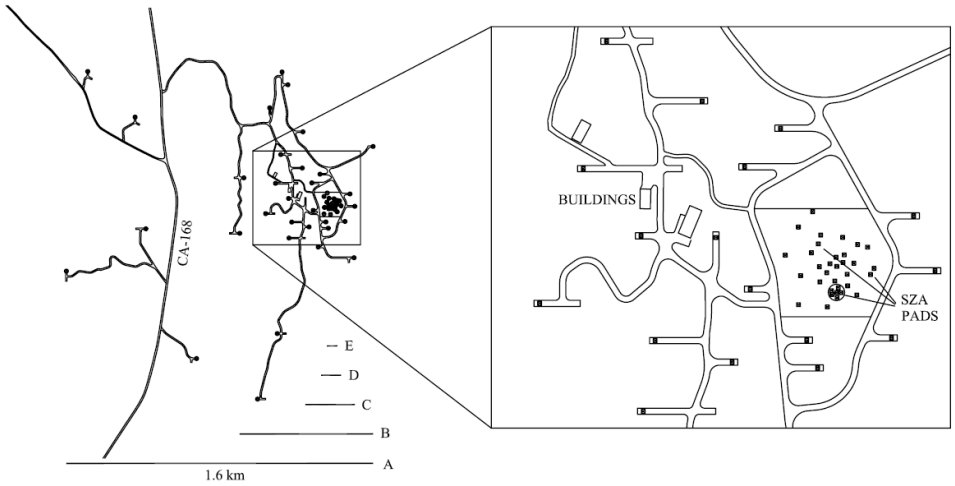

Figure 1.3: The layout of antenna pads for CARMA and a visual of the extent of each configuration (Bock, 2006).

resolutions (i.e. the HPBW of the synthesized beam) for each of CARMA's 5 configurations at 230 GHz, in Table 1.2. We also list the largest angular scale that can be imaged at 230 GHz as this is an important property of each configuration, especially when imaging extended emission (i.e., Chapter **??**). This limitation

is unique to interferometers and means that structures on angular scales significantly larger than the fringe spacing formed by the shortest baseline are not measured. This information can only be obtained by observing in a smaller array configuration or by using the mosaicing method. The half-power beamwidth of the primary beam (i.e., the FOV) at a frequency ν is $50'' \times (230\,\mathrm{GHz}/\nu)$ for the 6.1 m antennas, while is $30 \times''(230\,\mathrm{GHz}/\nu)$ for the 10.4 m antennas.

Table 1.2: Properties of the 5 CARMA configurations.

	A	B	C	D	E
B_{max} (m)	1883	946	370	148	66
B_{min} (m)	150	82	26	11	8.5
Synthesized Beam θ_{HPBW} ($''$)	0.15	0.38	0.86	2.1	4.4
Largest Angular Scale θ_{LAS} ($''$)	1.1	2.0	6.2	14.6	18.9
6.1 m Primary Beam θ_{HPBW} ($''$)	$50 \times''(230\,\mathrm{GHz}/\nu)$				
10.4 m Primary Beam θ_{HPBW} ($''$)	$30'' \times (230\,\mathrm{GHz}/\nu)$				

The 10.4 meter and 6.1 meter antennas are equipped with circular polarization SIS receivers for the 1mm band, and single-polarization SIS receivers for the 3 mm band. The tuning ranges of the 1mm and 3mm receivers are 215-265 GHz and 85-116 GHz, respectively. Figure 1.4 shows the main components in the signal path through the CARMA system. Upon passing through the atmosphere and antenna Naysmith optics, the RF signal is sent through the cooled low noise double sideband mixer where it is combined with a local oscillator ν_{LO1} to produce the intermediate frequency ν_{IF}. The ν_{LO1} can be either below or above the ν_{RF}; known as the upper and lower sidebands, respectively, giving:

$$\nu_{\mathrm{IF}} = \nu_{\mathrm{RF}} \pm \nu_{\mathrm{LO1}}. \tag{1.1}$$

The radio frequency gain $G_{\mathrm{RF}}(\nu_{RF})$, results from components before this mixer (i.e., the sky and antenna optics) and depends only on the sky frequency. The IF signals then pass through amplifiers and attenuators in the antenna, are converted to light and sent along fibers to the control building, where they are then

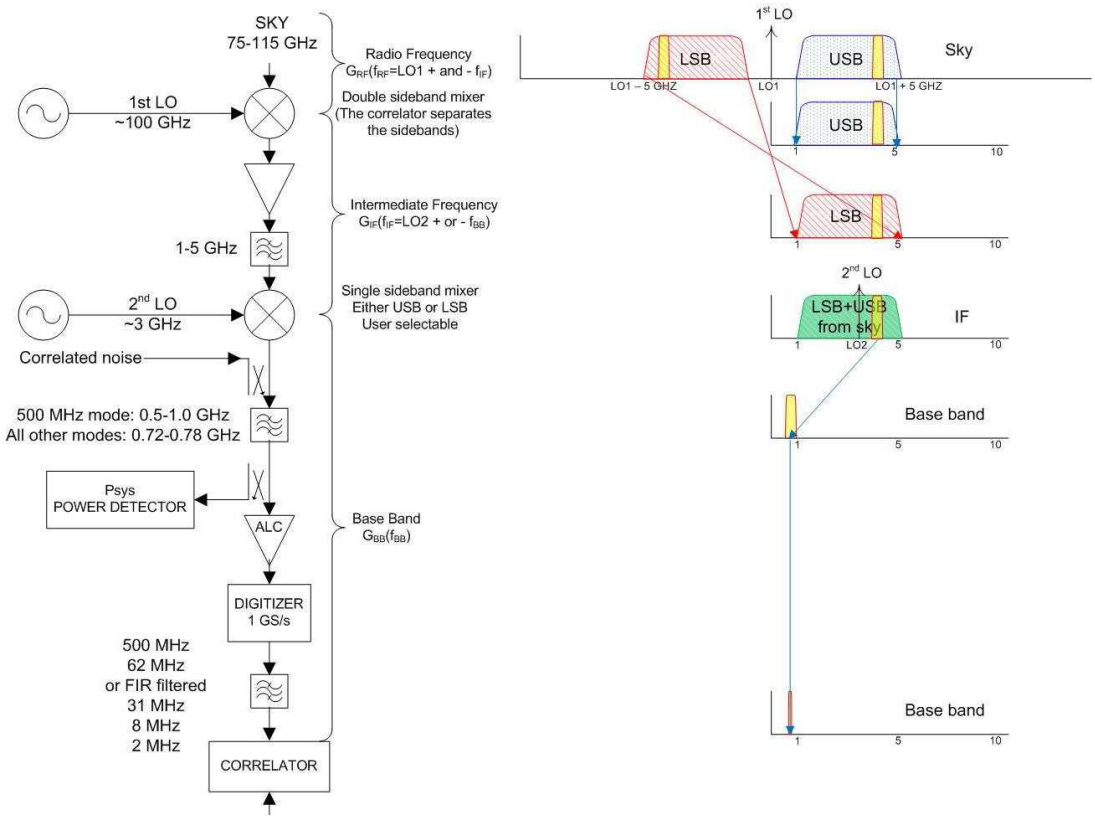

Figure 1.4: Major components in the signal path through the CARMA system (Wei *et al.*, 2008).

converted back to microwaves, amplified and attenuated some more before reaching the second mixer. Even though many of the components in the IF path are common across all bands, the IF gain $G_{\rm IF}(\nu_{\rm IF}\ )$, will vary per band as there are components in the second mixer which are separate for each band. The second mixer is a single sideband mixer and its baseband output contains either the upper sideband signals above the second LO or the lower sideband:

$$\nu_{\rm BB} = \nu_{\rm IF} \pm \nu_{\rm LO2}. \tag{1.2}$$

A noise signal is passed through all of the remaining correlator configuration dependent components and the selectable analog filters are measured by this noise source. The power measurement $P_{\rm sys}$, used for the system noise temperature measurement is calculated after the analog filters and before the automatic level

control (ALC) amplifier which ensures that the digitizers operate at a constant level.

1.3 CARMA Observations of Betelgeuse

We used CARMA to obtain on-source profiles of the rotational transition line $^{12}C^{16}O(J = 2\text{-}1)$ which has a rest frequency of 230.538 GHz (1.3 mm). Table 1.3 summarizes our complete set of multi-configuration observations which span the period 2007 May - 2009 November. Our first set of observations took place in June 2007 when CARMA was in D configuration providing a spatial resolution of 2.1″. A total of 5 D configuration tracks were carried out and one which took place in 18 May 2007 was excluded from the final analysis due to large levels of noise in the final map as a result of poor weather conditions. We obtained five E configuration (the most compact configuration available) tracks during the summer of 2009 which provided a relatively low spatial resolution of 4.4″ but gave the best sensitivity to extended emission. However, only one track was found to be of sufficient quality to be included in the final analysis. Our C configuration observations which provide sub-arcsecond resolution at 230 GHz (i.e., 0.9″) were due to take place in December 2008 but were postponed for a full year due to very poor weather conditions at Cedar Flat. We obtained a total of 4 usable tracks in C configuration amounting to 8.4 hours on source. The FOV of the individual 10.4 m antennas is $\sim 32''$ at the observed frequency.

CARMA can now take measurements in eight bands yielding a maximum bandwidth of 4 GHz per sideband. However, back when our data was obtained, the CARMA correlator took measurements in just three separate bands, each having an upper and lower sideband. One band was set to the low resolution 468 MHz bandwidth mode (15 channels of 31.25 MHz each) to observe continuum emission and was centered on the line. The other two bands were configured with 62 MHz and 31 MHz bandwidth across 63 channels (with a resolution of 1.3 km s^{-1} and 0.65 km s^{-1} respectively) and were also centered on the line. The line was measured in the upper sideband in the C and E array and in the lower sideband in the D array.

Bandpass and phase calibration were performed using 3C120 and 0530+135. 0532+075 was used as a secondary phase calibrator to determine the quality of the phase transfer from the primary phase calibrator. The observing sequence was to integrate on the primary phase calibrator for $\sim$ 2.5 minutes, the target for $\sim$ 18 minutes, and the secondary phase calibrator for $\sim$ 2.5 minutes. The cycle was repeated for each track which lasted between 1.5 hours and 5 hours. Absolute flux calibration was carried out with 0530+135 and 3C120 using the continuously updated CARMA flux catalog to obtain their flux values at each observation.

Table 1.3: CARMA Observations of α Ori between June 2007 and November 2009.

Date	Configuration	Time on Source (hr)	Flux Calibrator	Phase Calibrator	Image Cube Dynamic Range
2007 Jun 18	D	0.9	0530+135	0530+135, 0532+075	22.8
2007 Jun 21	D	3.0	0530+135	0530+135, 0532+075	22.7
2007 Jun 24	D	2.1	0530+135	0530+135, 0532+075	26.1
2007 Jun 25	D	2.4	0530+135	0530+135, 0532+075	30.2
2009 Jul 07	E	3.2	3C120	3C120, 0532+075	30.1
2009 Nov 05	C	1.2	3C120	3C120, 0532+075	17.3
2009 Nov 09	C	3.0	3C120	3C120, 0532+075	27.2
2009 Nov 15	C	1.0	3C120	3C120, 0532+075	17.8
2009 Nov 16	C	3.2	3C120	3C120, 0532+075	32.0
All	C	8.4	...	...	43.8
All	D	8.4	...	...	31.9
All	Multi-configuration	20.0	...	...	52.3

1.4 Arcturus and Aldebaran

Currently the most detailed spatial information about the atmospheres of K and early M spectral type evolved stars is obtained from eclipsing binaries such as the ζ Aurigae and symbiotic systems (e.g., Wright 1970; Baade *et al.* 1996; Eaton 2008; Crowley *et al.* 2008). Even though these systems offer us the best opportunity to obtain information on the dynamics and thermodynamics at various heights in the evolved star's atmosphere, the very nature of the binary system may introduce further complexities. For example, the orbital separation is often within the wind acceleration region and one could expect flow perturbations to be present (e.g., Chapman 1981). Using the old VLA, Harper *et al.* (2005) find a slow wind acceleration for ζ Aurigae and confirm that its velocity structure is not typical of single stars with similar spectral types, such as λ Velorum (Carpenter *et al.*, 1999). In order to avoid the assumed additional complexities of a companion, we have selected two single luminosity class III red giants: Arcturus (α Boo: K2 III) and Aldebaren (α Tau: K5 III). These nearby red giants have been extensively studied at other wavelengths and their stellar parameters, which are summarized in Table 1.4, are accurately known. These stars are predicted to be point sources at all frequencies between 1 and 50 GHz in all VLA configurations so our radio observations measure their total flux density, F_ν. For example, our observations of these stars which are discussed in Section 1.6, were taken in B configuration providing a maximum spatial resolution of $\sim 0.14''$ at 45 GHz which is equivalent to $\sim 7\ R_\star$ for both stars. The radio emission from these stars at 45 GHz is expected to be chromospheric in origin (Harper *et al.*, 2013), and as the spatial extent of red giant chromospheres is expected to be less than 1.5 $R_\star$ (Berio *et al.*, 2011), then we can be assured that these targets will be unresolved even at the highest VLA frequencies. Moreover, both stars have existing semi-empirical 1-D chromospheric and wind models which we can directly compare our data against.

Arcturus (α Boo: K2 III)

Arcturus (α Boo: K2 III) is the nearest ($d = 11.3$ pc) and brightest ($V = -0.04$ mag) noncoronal red giant and is probably the best example of a red giant whose

atmosphere can be studied in detail with the VLA. It is the leader of a group of stars that share a similar V space velocity (the component of stellar motion relative to the LSR in the direction of rotation), age ($\geq$ 10 Gyr), and metallicity ([Fe/H] ~ -0.5), known as the Arcturus moving group (Eggen, 1971). The group has traditionally been regarded as the remains of a dissolved open cluster (e.g., Eggen, 1971, 1996) but it has also been suggested to be the debris of a metal-poor accreted satellite some billions of years ago (Navarro *et al.*, 2004). Recent analysis of chemical abundances are consistent with the former hypothesis but do not entirely rule out a merger one (Williams *et al.*, 2009). Arcturus is ascending the red giant branch and being a single star, its mass is relatively poorly constrained but is similar to that of the Sun ($0.8 \pm 0.2\ M_{\odot}$ by Kallinger *et al.*, 2010). During the last decade there has been a large dispersion in the reported values of Arcturus' effective temperature (a nice graph summarizing this is presented in Griffin, 1996) but nowadays it is generally accepted to be about 4300 K (di Benedetto, 1993). A number of interferometric measurements of the limb-darkened angular diameter of the star are available in the literature with most values agreeing within their uncertainties. The weighted mean value of these values is $\theta_{\rm LD} = 21.06 \pm 0.17$ mas (Ramírez & Allende Prieto, 2011) giving the star a radius of $25.4 \pm 0.3\ R_{\odot}$.

Arcturus is an important target for high spatial and spectral resolution calibration. Thus when the Hipparcos catalog flagged Arcturus as a two component object (Perryman *et al.*, 1997) it caused quite a stir in the community. However, the uncertainties in the Hipparcos data (Soderhjelm & Mignard, 1998) along with a non-detection in adaptive optics observations (Turner *et al.*, 1999) and sensitive interferometric techniques (Lacour *et al.*, 2008) suggest that Arcturus is single and can still be used as a calibrator. Nevertheless, Lacour *et al.* (2008) still do not rule out the possibility of a planetary companion of a few Jovian masses as suggested by its long period radial velocity variations of $\sim$ 233 days (Brown, 2007; Hatzes & Cochran, 1993). Variations in the order of a few days period are also seen in its radial velocity (Merline, 1999) as well as photometry (Retter *et al.*, 2003). The photometric amplitude oscillations can vary by up to a percent and may be the manifestation of convection such as large-scale granulation, or solar-like oscillations (Dziembowski *et al.*, 2001).

The first detailed model of the atmosphere of Arcturus was the 1-D time-independent semi-empirical model of Ayres & Linsky (1975) which was based on diagnostics observable from the ground (i.e. Ca II h and k and the Ca II IR triplet) and early satellite observations of the Mg II h and k emission lines from *Copernicus*. They were able to calculate temperature and mass column densities

Table 1.4: Basic Properties of α Boo and α Tau.

Property	α Boo	α Tau	Reference
HD Number	124897	29139	...
Spectral Type	K2 III	K5 III	1
App. Mag. (V)	-0.5	0.86v	1
RA (ICRS: ep=J2000)	$14^{\rm h}15^{\rm m}39.672^{\rm s}$	$04^{\rm h}35^{\rm m}55.239^{\rm s}$	2
dec (ICRS: ep=J2000)	$+19°10'56.673''$	$+16°30'33.489''$	2
Proper motion-RA (mas yr^{-1})	-1093.39 ± 0.44	63.45 ± 0.84	2
Proper motion-dec (mas yr^{-1})	-2000.06 ± 0.39	-188.94 ± 0.65	2
π (mas)	88.83 ± 0.54	48.94 ± 0.77	2
d (pc)	11.3 ± 0.1	20.4 ± 0.3	2
$M_\star$ ($M_\odot$)	0.8 ± 0.2	1.3 ± 0.3	3, 4
$\theta_{\rm LD}$ (mas)	21.06 ± 0.17	20.58 ± 0.03	5, 6
$R_\star$ ($R_\odot$)	25.4 ± 0.3	44.2 ± 0.9	...
$T_{\rm eff}$ (K)	4294 ± 30	3970 ± 49	7
$L_\star/L_\odot$	198 ± 3	442 ± 11	...
$g_\star$ (cm s^{-2})	34	18	...
Heliocentric $v_{\rm rad}$ (km s^{-1})	$+5.19 \pm 0.04$	$+54.11 \pm 0.04$	8
$v_{\rm esc}$ (km s^{-1})	110	106	...
v_∞ (km s^{-1})	$35 - 40$	30	9, 10
$T_{\rm wind}$ (K)	$\sim$10,000	$\sim$10,000	9, 10
$\dot{M}_\star$ ($M_\odot$ yr^{-1})	2×10^{-10}	1.6×10^{-11}	9, 10
Photospheric $H_\star$ ($R_\star$)	0.005	0.005	...
Fe/H	-0.5 ± 0.2	-0.15 ± 0.2	11
Rotational period (yr)	2.0 ± 0.2	1.8	12, 13
$B_\star$ (G)	0.65 ± 0.26	unknown	14
Chromosphere Model	Drake (1985)	McMurry (1999)	...
Wind Model	Drake (1985)	Robinson *et al.* (1998)	...

References.-(1) Perryman *et al.* (1997); (2) van Leeuwen (2007); (3) Kallinger *et al.* (2010); (4) Lebzelter *et al.* (2012) (5) Ramírez & Allende Prieto (2011) (6) Richichi & Roccatagliata (2005); (7) di Benedetto (1993); (8) Massarotti *et al.* (2008); (9) Drake (1985); (10) Robinson *et al.* (1998); (11) Decin *et al.* (2003); (12) Gray *et al.* (2006); (13) Hatzes & Cochran (1993); (14) Sennhauser & Berdyugina (2011)

for the upper photosphere and chromosphere and estimated the temperature at the top of the chromosphere to be $\sim$ 8000 K. They also found that $T_{\rm min}/T_{\rm eff} \sim 0.77$ which is similar to that of the Sun. The important IUE cool star survey by Linsky & Haisch (1979) placed Arcturus on the right of the dividing line. This meant that its atmosphere showed lines formed at temperatures no hotter than $10,000 - 20,000$ K, suggestive of a chromosphere only. However, they also developed a hot coronal wind model for the star and found it to be consistent with the absence of transition region material in the IUE data; that is, the high temperature transition region emission line fluxes could be below the detection limit. Drake (1985) developed a semi-empirical chromosphere and wind model for Arcturus based on the Mg II k emission line from the IUE and showed that its wind is very extended and estimated a mass loss rate of 2×10^{-10} $M_{\odot}$ yr^{-1}.

Evidence began to emerge that Arcturus actually falls into the class of late type stars known as hybrids when deeply exposed IUE echelle spectrograms showed the weak presence of the Si III] λ1892.0 feature, indicating the existence of a small amount of plasma at temperatures as hot as 6×10^4 K. Its hybrid status was confirmed when C IV and N V (indicative of temperatures $\sim 1 \times 10^5$ K) were detected with the HST STIS, and also with a tentative 3σ X-ray detection made with the Chandra X-Ray Observatory (Ayres *et al.*, 2003). It appears that Arcturus has been able to sustain a modest level of magnetic activity. In fact, three possible values for the mean longitudinal magnetic field (albeit weak: $B = 0.65 \pm 0.26, 0.43 \pm 0.16$, and -0.23 ± 0.20 G) have reportedly been detected on the star via the Zeeman effect (Sennhauser & Berdyugina, 2011), and a magnetic cycle with a period of $\geq$ 14 years has also been reported (Brown *et al.*, 2008).

Arcturus appears to have a thermally bifurcated chromosphere which consists of material within the chromosphere that is cooler than the surrounding chromospheric temperature minimum [i.e a CO-mosphere, Wiedemann *et al.* (1994)]. This suggests that the assumption in current semi-empirical chromospheric models of the *hot* UV emitting material having a filling factor of unity may not be correct. The more recent spectroscopic analysis of CO and H_2O transitions have confirmed the existence of cooler molecular *clouds* in the outer atmosphere of Arcturus (Ryde *et al.*, 2002; Tsuji, 2009).

Aldebaran (α Tau: K5 III)

At a distance of 20.4 pc, Aldebaran (α Tau: K5 III) is a nearby red giant and is one of the most easily recognizable stars from the northern and most of the southern hemisphere. Even though it is almost twice as far away as Arcturus, its large stellar radius ($R_\star = 44.2 \pm 0.9\ R_\odot$) gives it a comparable angular diameter ($\theta_{\rm LD} = 20.58 \pm 0.03$), and is therefore another excellent candidate for multi-frequency studies with the VLA. Its effective temperature ($T_{\rm eff} = 3970 \pm 49$ K) is slightly lower than Arcturus', and it also has a slightly higher mass ($M = 1.3 \pm 0.3\ M_\odot$). Using these values for its radius and mass gives a surface gravity of $g_\star = 18$ (in units of cm s^{-2}), about 1500 times lower than the Sun's. The metallicity of Aldebaran is marginally subsolar with [Fe/H] $= -0.15 \pm 0.2$ (Decin *et al.*, 2003). Using high spectral resolution in the H, K, and L bands, Tsuji (2008) derived the carbon, nitrogen, and oxygen abundances in Aldebaran which suggests the mixing of the CN-cycled material in the first dredge-up. A 643 day period in the radial velocity for Aldebaran was reported by Hatzes & Cochran (1993), and Hatzes & Cochran (1998) find evidence to support the hypothesis that this variability comes from the reflex motion of the central star due to a planetary companion having a mass of 11 $M_{\rm Jup}$ although this has not been confirmed to date.

Aldebaran has been extensively studied at UV wavelengths. Early IUE observations placed the star well to the noncornal side of the Linsky-Haisch dividing line (Linsky & Haisch, 1979). The first chromospheric model of the star was developed in the late 1970s (Kelch *et al.*, 1978) and was based on both optical (mainly Ca II H and K) and UV (Mg II h and k) emission line fluxes. Later, GHRS spectra revealed the presence of significant flux in the C IV resonance lines around 1550 Å (Carpenter & Robinson, 1996), indicating the presence of some *hot* transition region plasma. In light of the new GHRS findings, a new model of the chromosphere and transition region of Aldebaran was developed, with temperatures reaching up to $T_e \sim 1 \times 10^5$ K. Modelling the GHRS optically thick Mg II and O I resonance lines (which show typical stellar wind absoption features), Robinson *et al.* (1998) found evidence for the acceleration of a slow wind and derived a mass-loss rate of $1.6 \times 10^{-11}\ M_\odot$ yr^{-1} and a terminal wind velocity of 30 km s^{-1}. Unexpectedly, FUSE spectra revealed revealed the presence (albeit weak)

of the coronal proxy O VI 1032 and 1038 Å emission lines (Dupree *et al.*, 2005) although Ayres *et al.* (2003) failed to detect any X-ray emission from the star. Like Arcturus, Aldebaran appears to harbour small levels of magnetic activity.

Wiedemann *et al.* (1994) observed Aldebaran's infrared ro-vibration absorption lines ($v = 2-1$) and matched them with synthetic spectra based on a model containing the semi-empirical photosphere of Kelch *et al.* (1978) and the best fitting temperature and column density profiles. Like Arcturus, they found a steady decrease in temperature with height, with the chromospheric temperature being constantly below the temperature minimum ($T_{\rm e}^{\rm min} \sim 2800$ K) of the Kelch model. Again, they explained their results by suggesting the existence of an extra *cool* component with a large ($> 99\%$) filling factor in the outer atmosphere (i.e. a thermally bifurcated CO-mosphere). Recently, Ohnaka observed the CO first overtone lines ($v = 2-0$) of Arcturus near 2.3 μm with the Very Large Telescope Interferometer (VLTI) and discovered a CO layer extending out to 2.5 $R_\star \pm 0.3$ $R_\star$. They were unable to constrain the geometrical thickness of of this CO layer from their data but we will show how our VLA radio data can constrain this value in Chapter 6. H_2O was also confirmed in its MOLsphere when Tsuji (2001) detected a H_2O absorption feature at ~ 6.6 μm. A narrow absorbtion feature in the midst of the wind absorption of the GHRS Mg II h and k lines has been interpreted and modelled as a feature of α Tau's wind-ISM interaction region also known as its astrosphere (Wood *et al.*, 2007).

1.5 The Karl G. Jansky Very Large Array

The NRAO[1] Karl G. Jansky Very Large Array (VLA) is an aperture synthesis radio telescope located on the Plains of San Agustin, New Mexico, USA and is capable of producing radio images with a spatial resolution greater than that of the HST. It is the product of a program to modernize the electronics of the old VLA which had been in operation at the same site since the late 1970's. One of the main upgrades to the VLA is the addition of the Wideband Interferometric Digital Architecture (WIDAR) correlator which allows the digital correlation of

[1]The National Radio Astronomy Observatory is a facility of the National Science Foundation operated under cooperative agreement by Associated Universities, Inc.

Table 1.5: Improved Performance Parameters of the VLA.

Parameter	old VLA	VLA	Improvement Factor
Continuum sensitivity (1σ, 9 hr)	10 μJy	1 μJy	10
Bandwidth per polarization	0.1 GHz	8 GHz	80
Coarsest frequency resolution	50 MHz	2 MHz	25
Finest frequency resolution	381 Hz	0.12 Hz	3180
Channels at max. bandwidth	16	16,384	1024
Maximum number of channels	512	4,194,304	8192

very wideband signals. WIDAR digitally filters and splits the data into sub-bands which are then separately cross correlated and integrated before being stitched together again to yield the final wideband spectrum. The new WIDAR correlator and its superior bandwidth capability provides the VLA with greater sensitivity, allowing the detection of lower flux density sources than was previously possible with the old VLA. A comparison of the performance parameters of the VLA with those of the old VLA is shown in Table 1.5. The three major new observational abilities of the VLA are:

1. Complete frequency coverage between 1 and 50 GHz opening up new regions of the electromagnetic spectrum to astronomy.

2. An increase in continuum sensitivity by an order of magnitude at some frequencies, by increasing the bandwidth to 8 GHz per polarization.

3. Process the large bandwidth with a minimum of 16,384 spectral channels per baseline.

Apart from the addition of more feeds at the center of the reflector, the structural design of the VLA has not changed during its recent upgrade. As before it consists of 27 fully steerable alt-azimuth antennas arranged along the arms of an upside-down 'Y' as shown in Figure **??**. The array is re-configurable and can vary its resolution by over a factor of ~ 50 through movement of its component antennas along twin railroad tracks. Four standard configurations of antennas along the arms of the array are possible whose scales vary by the ratios 1 : 3.28

: 10.8 : 35.5 from smallest to largest. These are called D, C, B, and A configurations, with A having the longest baselines ($\sim$ 36 km) giving the best spatial resolution, but lacking short baselines needed for imaging extended structure. In each configuration, the distance of each antenna from the center of the 'Y' is equal to $m^{\ln 2}$ where m is the antenna location number, counting outwards from the center of each arm. With this design, the m'th station in any configuration coincides with the $2m$'th station in the next smaller configuration. This means that only 72 stations are needed to handle all four configurations. Additionally, there are 3 hybrid configurations called DnC, CnB, and BnA, which are well suited for sources with low declination. In these configurations, the North arm antennas are deployed in the next larger configuration than the SE and SW arm antennas resulting in a more circular synthesized beam for these sources.

Each antenna is 25 m in diameter giving the array a total collecting area equivalent to a single dish of 130 m in diameter. Each antenna has an off-axis Cassegrain design with a rotatable sub-reflector at the prime focus of the main reflector and is supported by four feed legs as shown in Figure 1.5. All feeds are located on a feed ring at the Cassegrain focus and the observing feed is changed by rotating the asymmetric sub-reflector about the main reflector axis so that the secondary focal point moves to the desired feed. The standard observing mode for all feeds is circular polarization. RF signals from each feed are sent via a waveguide to the antenna vortex room located directly underneath the main reflector where they are feed into low noise front ends. The vortex room is temperature controlled and also contains cryogenic cooling systems for the front end, portions of the LO, and IF equipment. IF signals from each antenna are sent by cable to a shielded room where the signals are cross correlated.

All VLA antennas are outfitted with eight receivers providing continuous frequency coverage between 1 and 50 GHz. As shown in Table 1.6, the frequency ranges of 1-2 GHz, 2-4 GHz, 4-8 GHz, 8-12 GHz, 12-18 GHz, 18-26.5 GHz, 26.5-40 GHz, and 40-50 GHz, are commonly referred to as L, S, C, X, Ku, K, Ka, and Q bands, respectively. Additionally, the VLA is currently being outfitted with even lower frequency receivers, P-band (230-470 MHz) and 4-band (54-86 MHz). The VLA's spatial resolution is set by the maximum baseline $B_{\rm max}$ and frequency of observation. This means that structures smaller than the diffraction

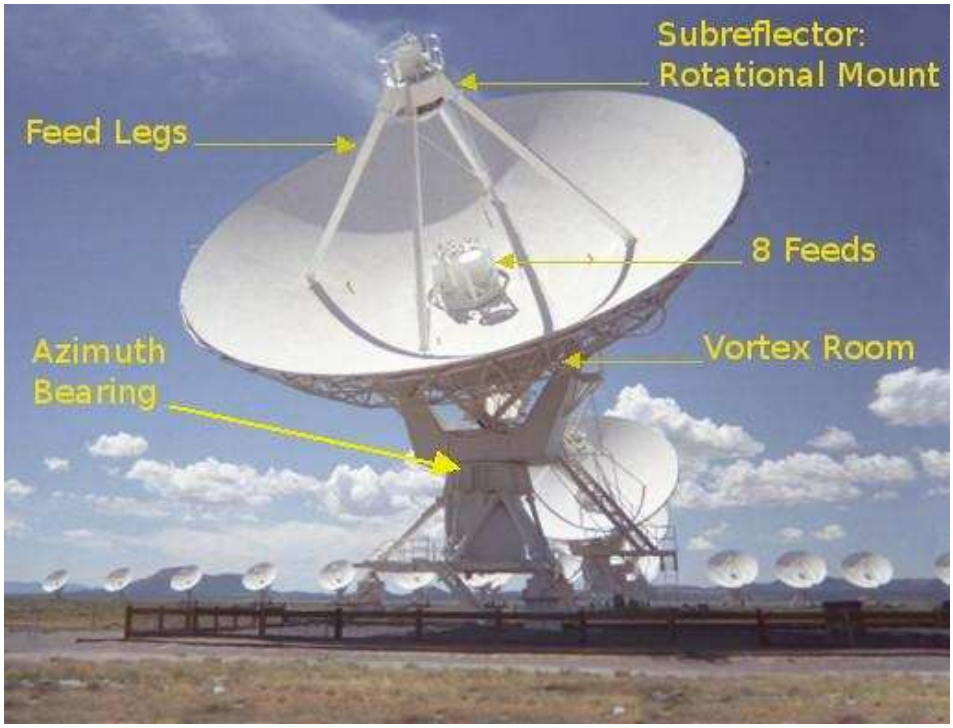

Figure 1.5: Main features of a VLA antenna. The sub-reflector is located at prime focus on a rotational mount is supported by four feed legs. The 8 feeds are located in a ring at the secondary focus. The feeds send the RF signal to the front end located in the vortex room directly beneath the main reflector. *Image Credits:* NRAO/AUI.

limit ($\theta_{\rm HPBW} \sim \lambda/B_{\rm max}$) will be smoothed to the resolution of the array. Table 1.6 also summarizes the maximum resolution for each of the four main configurations at each wavelength. The resolution is defined here as the HPBW of the synthesized beam, using uniform weighting, over a full 12 hour synthesis observation of a source which passes near the zenith. For completeness, we also give the field of view (FOV) at each observing frequency in Table 1.6, defined as the HPBW of the primary beam, which for the VLA antennas can be approximated using the formula: FOV($'$) $= 45/\nu_{\rm GHz}$.

Table 1.6: Frequency coverage, primary beam, and spatial resolution of the VLA.

	L	S	C	X	Ku	K	Ka	Q
ν (GHz)	1.5	3.0	6.0	10	15	22	33	45
λ (cm)	20	13	6.0	3.0	2.0	1.3	1.0	0.7
ν Range (GHz)	1-2	2-4	4-8	8-12	12-18	18-26.5	26.5-40	40-50
A config: $\theta_{\rm HPBW}$ ($''$)	1.3	0.65	0.33	0.20	0.13	0.089	0.059	0.043
B config: $\theta_{\rm HPBW}$ ($''$)	4.3	2.1	1.0	0.6	0.42	0.28	0.19	0.14
C config: $\theta_{\rm HPBW}$ ($''$)	14	7.0	3.5	2.1	1.4	0.95	0.63	0.47
D config: $\theta_{\rm HPBW}$ ($''$)	46	23	12	7.2	4.6	3.1	2.1	1.5
FOV($'$)	30	15	7.5	4.5	3.0	2.0	1.4	1.0

1.6 VLA Observations of Arcturus and Aldebaran

The Open Shared Risk Observing (OSRO) program at the VLA existed during its commissioning phase to provide observers with early access to a number of VLA correlator capabilities and observing modes. This represented a considerable improvement over the capabilities of the old VLA correlator as observes were provided with increased bandwidth capability at existing VLA bands, increased spectral resolution capabilities, and access to new spectral bands. In September 2010 our proposal (PI: G. M. Harper, Program ID: 10C-105) to observe two archetypical red giants at multiple frequencies was allocated the requested 15.5 hours of observing time with the VLA as part of NRAO's OSRO Science Program 2010C. A number of observing scripts called scheduling blocks (SBs) were prepared during December 2010 and their duration were kept to ≤ 2.5 hours to increase their likelihood of been scheduled. The VLA now uses dynamic scheduling for deciding which SBs are executed at any time. This takes into account many factors like the scheduling priority assigned by the time allocation committee, weather constraints, and SB duration. Dynamic scheduling means that the observer does not know when their observations will occur but in general, the chances of observations being scheduled are increased if the duration of the SB is kept short.

Table 1.7: VLA Observations of α Boo and α Tau obtained in February 2011 and July 2012.

Star	Date	Band	ν (GHz)	λ (cm)	Time on Star (hr)	Restoring Beam ($''\times''$)	Bandwidth (GHz)	Number of Antennas	Phase Calibrator
α Boo	2011 Feb 22	Q	43.3	0.7	0.3	0.19×0.15	0.256	22	J1357+1919
	2011 Feb 22	Ka	33.6	0.9	0.2	0.25×0.20	0.256	23	J1357+1919
	2011 Feb 22	K	22.5	1.3	0.4	0.35×0.28	0.256	24	J1357+1919
	2011 Feb 11	X	8.5	3.5	0.3	1.14×0.70	0.256	18	J1415+1320
	2011 Feb 11	C	5.0	6.0	0.5	2.02×1.30	0.256	21	J1415+1320
	2011 Feb 13	S	3.1	9.5	1.8	2.57×2.08	0.256	12	J1415+1320
	2012 Jul 19	S	3.0	10.0	0.7	2.82×2.30	2.0	23	J1415+1320
	2012 Jul 20	L	1.5	20.0	1.6	4.46×3.94	1.0	23	J1415+1320
α Tau	2011 Feb 11	Q	43.3	0.7	0.3	0.18×0.16	0.256	22	J0431+1731
	2011 Feb 11	Ka	33.6	0.9	0.2	0.22×0.20	0.256	19	J0449+1121
	2011 Feb 11	K	22.5	1.3	0.4	0.35×0.31	0.256	21	J0449+1121
	2011 Feb 13	X	8.5	3.5	0.5	0.85×0.78	0.256	25	J0449+1121
	2011 Feb 13	C	5.0	6.0	1.2	1.48×1.32	0.256	21	J0449+1121
	2011 Feb 12	S	3.1	9.5	1.8	2.74×2.02	0.256	11	J0431+2037

Our main set of observations took place in February 2011 while the VLA was in B configuration. All observations were taken in continuum mode and the correlator was set up with two 128 MHz sub-bands centered on the frequencies listed in Table 1.7. Each sub-band had sixty-four channels of width 2 MHz and four polarization products (RR, LL, RL, LR). We obtained all our requested observations of α Tau in just two days between the 11$^{\rm th}$ and 13$^{\rm th}$ of February 2011 which consisted of Q, Ka, K, X, C, and S band observations of the star. We did not request L band (i.e. 1.5 GHz) observations of α Tau as it was believed that the star would be too faint to be observable at this frequency. There was also insufficient Ku band receivers available at the time to carry out observations at 15 GHz. We obtained Q, Ka, K, X, C, and S band observations of α Boo in eleven days between the 11$^{\rm th}$ and 22$^{\rm nd}$ of February 2011. We also had prepared a 2.5 hour SB for α Boo at L-band but this SB was never executed.

For this reason we applied for (and were awarded) 3 additional hours of directors discretionary time (DDT) in early 2012 (PI: E. O'Gorman, Program ID: 12A-472) to observe α Boo at S and L band. We decided to include a short observation at S band even though we already had an observation at this band to make sure that the stars flux density had not significantly changed over that period and so any possible L band detection could be included in the analysis of the main set of data from the previous year. Our DDT observations took place in July 2012 when the VLA was again in B configuration with details given in Table 1.7. The capabilities of the VLA had greatly increased in the $\sim$ 1.5 years since the main set of observations and we now could utilize the full 1 and 2 GHz of bandwidth at L and S band, respectively. The 1-2 GHz and 2-4 GHz frequency ranges were both divided into 16 sub-bands, each with sixty-four channels. The channel width was 2 and 1 MHz for S and L-band, respectively, and each sub-band had four polarization products (RR, LL, RL, LR).

In radio interferometry, baseline-dependent additive errors in the visibilities can occasionally lead to artifacts occurring at phase center of the final image. Such errors may be caused by unflagged low level interference picked up by some antennas baselines. An example of this is demonstrated in Figure 1.6 in which two radio images of Betelgeuse at 15 GHz are shown (A. Brown, priv. comm.). The left panel was taken on 2$^{\rm nd}$ February 2002 and shows a 30σ detection of Betelgeuse

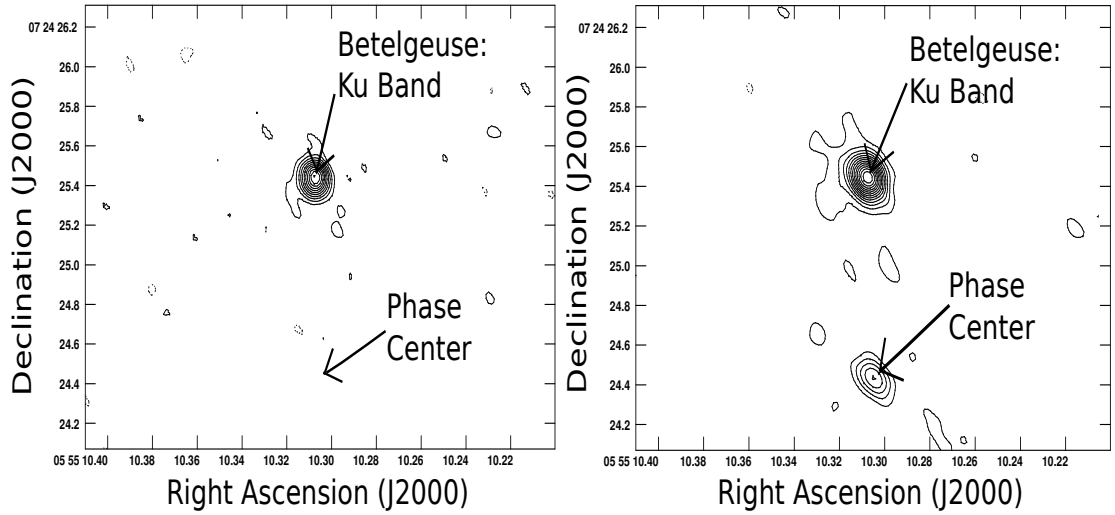

Figure 1.6: An example to highlight the importance of offsetting the source from phase center. *Left:* Old VLA image of Betelgeuse at 15 GHz taken on showing no source at the phase center of the image. Contour levels at σ(-6,-3,3,....30) where σ = 84 μJy. *Right:* Two months later Betelgeuse was again image at 15 GHz but now shows a strong artifact at phase center. Contour levels at σ(-6,-3,3,....45) where $\sigma = 90$ μJy (A. Brown, priv. comm.).

with low level background noise. The right panel which was taken two months later on 2$^{\rm nd}$ April 2002 shows a 45σ detection of the star but also now shows a 15σ artifact at phase center. If the target had been observed at phase center in this case, then this artifact would lead to an incorrect flux density measurement for the star. For our VLA observations, both α Boo and α Tau were slightly offset from the phase-center by ~ 5 synthesized beam widths in order to avoid source contamination by these rare but possible phase center artifacts and therefore avoiding spurious detections.

The main problem at low VLA frequencies (L and S bands) is disturbances in the ionosphere caused by solar activity. At L-band, solar flares can be as strong as 1×10^6 Jy and are a major source of interference, with their effects sometimes being impossible to remove from the data. To avoid such problems the S and L band SBs were scheduled for night time observing only. The low to intermediate frequency observations (L - X bands) were composed of repeatedly interleaved observations of the target and a nearby phase calibrator with cycle times of 12 minutes; 10 minutes on the target and 2 minutes on the phase calibrator. For α

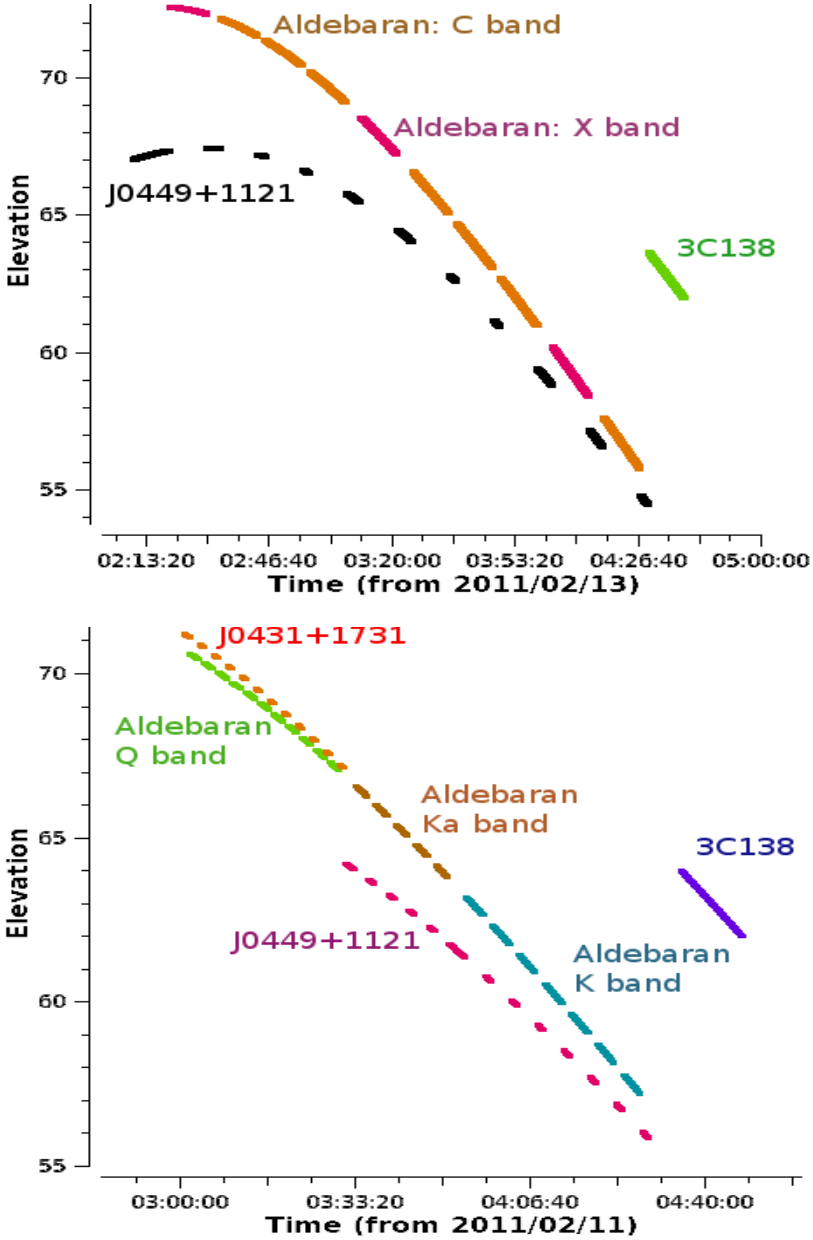

Figure 1.7: Overview of a low and high frequency VLA SB for α Tau. *Top Panel:* The low frequency observations consisted of interleaved observations of the target and a nearby phase calibrator with cycle times of 12 minutes. The X band observations were interspersed between C band observations to obtain a good spread in $u-v$ coverage. *Bottom Panel:* The high frequency observations had short cycle times to compensate for tropospheric effects. Q band observations were taken first to ensure the best pointing solutions were applied to them.

Boo, the point source J1415+1320 which is located 6° away was used as the phase calibrator at these frequencies. For α Tau, the point source J0449+1121 located 6° away was used at C and X band, while the brighter J0431+2037 located 4° away was used at S band due to it being unresolved at this frequency (but is resolved at C and X band). The primary calibration sources 3C286 and 3C138 were observed at the end of all low and intermediate frequency SBs and were used to measure the bandpass and set the absolute flux for α Boo and α Tau, respectively. The top panel in Figure 1.7 shows a plot of elevation against time for all the sources observed in the SB of the C and X band observations of α Tau. In this SB, observations of α Tau at X band were interspersed between C band observations throughout the track to obtain a good spread in $u - v$ coverage.

At high VLA frequencies (i.e. K, Ka, and Q band) the troposphere can cause major phase variations to incoming radio waves. To reduce this problem, the old VLA used a technique called *fast switching* which reduced the setup overhead and slewing compared to traditional iterating between source and calibrator scans. This overhead is sufficiently reduced with the new VLA and no special fast switching mode is necessary. Instead regular but short duration source-calibrator loops are implemented. As a result, the calibration overheads for high frequency observing are typically considerably larger than for lower frequency observations. For both stars, the total cycle times for the Q, Ka, and K-band observations were 160, 230, and 290 s, respectively. These high frequency observations were combined into a single 2 hour SB for each star and commenced with X-band reference pointing with solutions being applied on-line. As mentioned in Section **??**, the blind pointing errors of the VLA antennas can occasionally be as large as the HPBW of the primary beam at high frequencies. Thankfully, the pointing can be calibrated for using a technique known as *reference pointing* whereby a nearby known calibrator is observed in interferometer pointing mode every hour or so. The measured local pointing corrections are then be applied to subsequent target observations. Reference pointing can reduce the rms pointing errors to as little as 2″ if the reference source is with 10° of the target source. After X-band pointing the target source was observed at Q-band to ensure the best pointing solutions were used as shown in the lower panel of Figure 1.7 for α Tau.

1.7 VLA-Pie Town Observations of Betelgeuse

As part of our study into Betelgeuse's extended atmosphere we decided to re-visit some archival high spatial resolution VLA data from the early 2000's. This was motivated by the recent findings of Richards *et al.* (2013) who detected two hot chromospheric features with the very long baseline interferometer e-MERLIN. The two features, also referred to as 'hot spots', were found to have brightness temperatures well above the mean brightness temperature measured at the same radio wavelength, and were separated from each other by 90 mas. We wanted to see if these features were present at other wavelengths and if so, how they varied over time.

Asymmetries in Betelgeuse's atmosphere were first detected in the radio in old VLA-MERLIN combined images at 6 cm (Dr. Rhys Morris, personal communication, 2012 Dec 23) and at then confirmed by Lim *et al.* (1998) at 0.7 cm. To see how these asymmetries evolved with time, a multi-wavelength study into the temporal evolution of Betelgeuse's atmosphere was carried out with the old VLA over a number of years in the early 2000's in its most extended A configuration plus the Pie Town link[1]. This study focused on fitting various models to the visibility data as was done by Lim *et al.* (1998), i.e., the analysis was mainly carried out in the visibility plane. The detection of the two unique hot spots in the e-MERLIN radio maps by Richards *et al.* (2013) inspired us to revisit this data which, because of the addition of the Pie Town link to the VLA, gave spatial resolution comparable to or exceeding that of e-MERLIN at some wavelengths. Our goal was to carry out the analysis in the image plane to make a direct comparison with the findings of Richards *et al.* (2013). In Table 1.8 we summarize this unique data set which consists of almost four years of high resolution multi-wavelength observations of Betelgeuse. To increase our observational time period we also include the short wavelength high resolution (i.e., A configuration) observations of the star from 1998. Betelgeuse was resolved at all wavelengths listed in Table 1.8 except at L band.

The VLA-Pie Town Link

[1]This data was carefully calibrated by Dr. Alexander Brown.

Table 1.8: Multi-wavelength VLA + Pie Town Observations of Betelgeuse

Date	Band	λ (cm)	Time on Star (hr)	Restoring Beam (mas)	rms noise (mJy/beam)
2004 Oct 21,30	Q	0.7	1.2	39×26	0.37
	K	1.3	2.6	80×41	0.09
	U	2.0	3.3	121×91	0.08
	X	3.5	3.8	208×126	0.02
	C	6.2	2.9	377×265	0.02
	L	16.7	2.4	1262×889	0.03
2003 Aug 10,12	Q	0.7	0.9	40×27	0.46
	K	1.3	2.6	80×42	0.18
	U	2.0	3.3	119×96	0.10
	X	3.5	3.0	204×139	0.03
	C	6.2	2.8	378×297	0.03
	L	16.7	2.6	1247×931	0.04
2002 Feb 17,18	K	1.3	2.0	82×47	0.14
	U	2.0	2.0	128×90	0.11
	X	3.5	2.1	200×135	0.03
	C	6.2	1.6	372×273	0.3
	L	16.7	1.1	1312×951	0.05
2002 Apr 12,13	K	1.3	2.0	91×59	0.18
	U[a]	2.0	2.0	130×98	0.39
	X	3.5	2.1	224×154	0.03
	C[b]	6.2	1.6	406×295	0.3
	L	16.7	0.9	1397×1146	0.07
2001 Jan 02	K	1.3	6.0	78×42	0.08
2000 Dec 23	Q	0.7	6.0	44×20	0.18
1998 Mar 29,30	Q[c]	0.7	5.3	39×36	0.38
	K[c]	1.3	6.3	114×89	0.25

[a] Spurious source seen at phase center of image.
[b] The star was not detected in this data set.
[c] No Pie Town link was used in this data.

The 25 m antenna located at Pie Town, New Mexico is one of 10 antennas spread across the United States of America which together make up the Very Long Baseline Array (VLBA). It was successfully connected in real time via a 104 km long

fiber optic line to the VLA in 1999 and was operational at all old VLA frequencies prior to its upgrade to the Karl G. Jansky VLA. The Pie Town antenna is located approximately 52 km west of the center of the VLA, effectively doubling its resolution while in A configuration when connected. It is worth noting that the Pie Town link was only functional when the VLA was in A configuration. The extra collecting area together with 27 additional baselines also increases the sensitivity of the array. The Pie Town antenna generates IF signals in VLBA format and these are converted, at Pie Town, to a 50 MHz wide VLA signal where they are multiplexed and then modulated onto a single laser before being sent over 104 km of fiber to the VLA. When the signal arrives at the VLA site it is received and converted back into an RF signal. The received RF signal is then amplified and filtered before its is sent on to the backend receiver.

A

List of Abbreviations Used in this Thesis.

Table A.1: List of Abbreviations

First entry	Second entry
BIMA	Berkeley Illinois Maryland Association
CARMA	Combined Array for Research in Millimeter-wave Astronomy
CSE	Circumstellar Envelope
DDT	Director's Discretionary Time
e-MERLIN	e-Multi-Element Radio Linked Interferometer Network
FOV	Field of View
GREAT	German Receiver for Astronomy at Terahertz Frequencies
HPBW	Half Power Beamwidth
HST	Hubble Space Telescope
IOTA	Infrared Optical Telescope Array
IR	Infrared
IRAM	Institut de Radioastronomie Millimétrique
IUE	International Ultraviolet Explorer
LSR	Local Standard of Rest
MEM	Maximum Entropy Method
OVRO	Owens Valley Radio Observatory
RFI	Radio Frequency Interference
S/N	signal-to-noise ratio

Continued on next page

Table A.1 – *Continued from previous page*

First entry	**Second entry**
SOFIA	Stratospheric Observatory for Infrared Astronomy
SMA	Submillimeter Array
UV	Ultraviolet
VLA	Karl G. Jansky Very Large Array
VLBA	Very Long Baseline Array
VLT	Very Large Telescope

B

Discrete Absorption Feature

The temperature equation outlined in Chapter **??** assumes that the wind is homogenous, but this may not be the case for Arcturus. During this study we analyzed STIS spectra of Arcturus from the online StarCAT catalog (Ayres, 2010). The Mg II h and k lines from data obtained in 2001 show a wind velocity $\sim 30 - 40$ km s^{-1}, which is similar to that adopted in the Drake models for this star Drake (1985). A narrow discrete absorption feature is found at -49 km s^{-1} in the broad blue-shifted wind absorption component of both lines as shown in Figure B.1. For this discrete feature we find a most probable turbulent velocity of 3.4 km s^{-1} and a Mg column density[1] of 1.4×10^{12} cm^{-2}. A Mg column density of 10^{15} cm^{-2} is required to produce the blueward absorption components in the h and k lines (McClintock *et al.*, 1978). Therefore, this discrete absorption feature accounts for $\sim 0.1\%$ of the total wind column density.

[1] Assuming all Mg to be Mg II

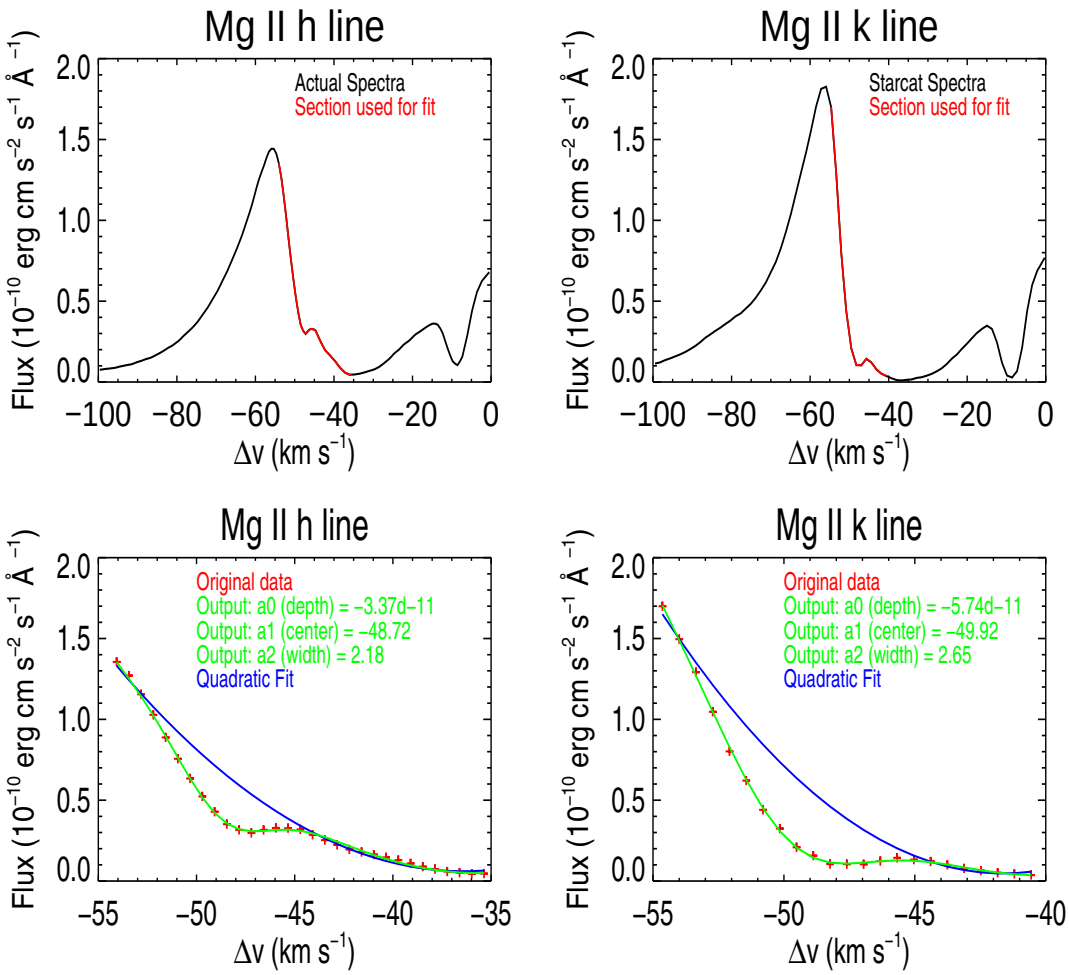

Figure B.1: Analysis on the absorption feature found in the Mg II h and k lines. A function composed of a linear combination of a Gaussian and a quadratic fitted the discrete absorption feature the best. The red data in the upper row shows the data that is used in this analysis.

C

Ambipolar Diffusion Heating

Considering a steady flow accelerating in an inertial frame, the equation of motion can be written as

$$\rho_n \boldsymbol{a}_n = \rho_n \boldsymbol{g} + \boldsymbol{f}_d \tag{C.1}$$

for the neutral species n, and

$$\rho_i \boldsymbol{a}_i = \rho_i \boldsymbol{g} - \boldsymbol{f}_d + \boldsymbol{f}_L \tag{C.2}$$

for the ion species, i. The flow acceleration is defined as $\boldsymbol{a} \equiv (\boldsymbol{v}.\nabla)\boldsymbol{v}$ and the gravitational acceleration is $\boldsymbol{g} \equiv \nabla(GM_\star/r)$. The volumetric drag force of the ions on the neutrals is defined as

$$\boldsymbol{f}_d = \gamma \rho_n \rho_i (\boldsymbol{v}_i - \boldsymbol{v}_n) \tag{C.3}$$

and $\boldsymbol{f}_L$ is the volumetric Lorentz force. The equation of motion for the combined ion-neutral fluid is found by addition of Equations C.1 and C.2

$$\rho \boldsymbol{a} = \rho \boldsymbol{g} + \boldsymbol{f}_L \tag{C.4}$$

where $\rho \equiv \rho_n + \rho_i$ is the mass density without the electrons and $\boldsymbol{a} \equiv (\rho_n \boldsymbol{a}_n + \rho_i \boldsymbol{a}_i)/\rho$ is the total acceleration.

The gravitational acceleration term can then be eliminated from Equations C.1 and C.2 to give

$$\boldsymbol{a}_n - \boldsymbol{a}_i = \left(\frac{1}{\rho_n} + \frac{1}{\rho_i}\right) \boldsymbol{f}_d - \frac{1}{\rho_i} \boldsymbol{f}_L. \tag{C.5}$$

Assuming then that the acceleration of the neutrals and ions are the same we get

$$\boldsymbol{f}_d = \left(\frac{\rho_n}{\rho_n + \rho_i}\right) \boldsymbol{f}_L. \tag{C.6}$$

This equation tells us that for a lightly ionized outflow the drag force is almost equal to the Lorentz force. We can now obtain an expression for the slip velocity, $\boldsymbol{w}$, by subbing this equation into Equation C.3

$$\boldsymbol{w} = \boldsymbol{v}_i - \boldsymbol{v}_n = \frac{\boldsymbol{f}_L}{\gamma \rho_i (\rho_n + \rho_n)}. \tag{C.7}$$

The slip velocity becomes large when the ion density becomes small, but does not become large when the neutral density becomes small because the large density of ions drag the few neutrals that are present along with the rest of the mostly ionized plasma. The heating rate per unit volume due to ambipolar diffusion heating is

$$\Gamma = \boldsymbol{f}_d . \boldsymbol{w} \tag{C.8}$$

and substitution of Equations C.6 and C.7 gives

$$\Gamma = \frac{\rho_n |\boldsymbol{f}_L|^2}{\gamma \rho_i (\rho_n + \rho_i)^2}, \tag{C.9}$$

and so for a completely ionized plasma, $\Gamma = 0$.

In order to calculate the ambipolar diffusion heating, we need to find a value for the ion-neutral momentum transfer coefficient, γ (in units $\mathrm{cm^3\,s^{-1}\,g^{-1}}$) which depends on the collisional coefficient rates, cross sections, slip speed, and gas

composition. Shang *et al.* (2002) give the following expression

$$\gamma = \frac{2.13 \times 10^{14}}{1 - 0.714 x_e} \left(\left[3.23 + 41.0 T_4^{0.5} \times \left(1 + 1.338 \times 10^{-3} \frac{w_5^2}{T_4} \right)^{0.5} \right] x_{HI} + 0.243 \right) \tag{C.10}$$

where T_4 is the temperature in units of $10^4\,\mathrm{K}$, w_5 is the slip speed in units of $\mathrm{km\,s^{-1}}$. We have assumed no molecular hydrogen to be present and the fractional abundance of He, $x_{He} = 0.1$. Subbing Equation C.7 into Equation C.10 gives a quartic equation for γ, i.e.,

$$\begin{aligned} \gamma^4 - (2AE + 2ABx_{HI})\gamma^3 + (A^2E^2 + 2A^2BEx_{HI} + \\ A^2B^2x_{HI}^2 - A^2C^2x_{HI}^2)\gamma^2 - GA^2C^2x_{HI}^2 = 0 \end{aligned}$$

where
$A = \frac{2.13\times10^{14}}{1-0.714x_e}$, $B = 3.23$, $C = 41.0T_4^{0.5}$, $D = \frac{1.338\times10^{-3}}{T_4}$, $E = 0.243$, $F = \frac{\boldsymbol{f}_L}{\rho_i(\rho_n+\rho_i)}$, and $G = \frac{DF^2}{1\times10^{10}}$. Finally the radial and azimuthal Lorentz forces and thus the corresponding volumetric ambipolar heating rates can be calculated by using the following expressions for the flow and gravitational accelerations:

$$\boldsymbol{a} = v\frac{dv}{dr}\boldsymbol{r} + \frac{v}{r}\frac{dv}{d\theta}\boldsymbol{\theta} + \frac{v}{r\sin\theta}\frac{dv}{d\phi}\boldsymbol{\phi} \tag{C.11}$$

and

$$\boldsymbol{g} = -\frac{GM_\star}{r^2}\boldsymbol{r} + \frac{1}{r}\frac{d}{d\theta}\left(\frac{GM_\star}{r}\right)\boldsymbol{\theta} + \frac{1}{r\sin\theta}\frac{d}{d\phi}\left(\frac{GM_\star}{r}\right)\boldsymbol{\phi}. \tag{C.12}$$

References

Ayres, T.R. (2010). StarCAT: A Catalog of Space Telescope Imaging Spectrograph Ultraviolet Echelle Spectra of Stars. *Astrophysical Journal Supplemental Series*, **187**, 149–171. (Cited on page 33.)

Ayres, T.R. & Linsky, J.L. (1975). Stellar model chromospheres. III - Arcturus /K2 III/. *Astrophysical Journal*, **200**, 660–674. (Cited on page 15.)

Ayres, T.R., Brown, A. & Harper, G.M. (2003). Buried Alive in the Coronal Graveyard. *Astrophysical Journal*, **598**, 610–625. (Cited on pages 16 and 18.)

Baade, R., Kirsch, T., Reimers, D., Toussaint, F., Bennett, P.D., Brown, A. & Harper, G.M. (1996). The Wind Outflow of zeta Aurigae: A Model Revision Using Hubble Space Telescope Spectra. *Astrophysical Journal*, **466**, 979. (Cited on page 13.)

Bedecarrax, I., Petit, P., Aurière, M., Grunhut, J., Wade, G., Chiavassa, A., Donati, J.F., Konstantinova-Antova, R. & Perrin, G. (2013). Long-term spectropolarimetric monitoring of the cool supergiant betelgeuse. In *EAS Publications Series*, vol. 60 of *EAS Publications Series*, 161–165. (Cited on pages 2 and 3.)

Berio, P., Merle, T., Thévenin, F., Bonneau, D., Mourard, D., Chesneau, O., Delaa, O., Ligi, R., Nardetto, N., Perraut, K., Pichon, B., Stee, P., Tallon-Bosc, I., Clausse, J.M., Spang, A., McAlister, H., ten Brummelaar, T., Sturmann, J., Sturmann, L., Turner, N., Farrington, C. & Goldfinger, P.J. (2011). Chromosphere of K giant stars. Geometrical extent and spatial structure detection. *Astronomy & Astrophysics*, **535**, A59. (Cited on page 13.)

Bernat, A.P., Hall, D.N.B., Hinkle, K.H. & Ridgway, S.T. (1979). Observations of CO circumstellar absorption in the 4.6 micron spectrum of Alpha Orionis. *Astrophysical Journal Letters*, **233**, L135–L139. (Cited on page 3.)

Bock, D.C.J. (2006). CARMA: Combined Array for Research in Millimeter-Wave Astronomy. In D.C. Backer, J.M. Moran & J.L. Turner, eds., *Revealing the Molecular Universe: One Antenna is Never Enough*, vol. 356 of *Astronomical Society of the Pacific Conference Series*, 17. (Cited on pages 6 and 7.)

Brown, K.I.T. (2007). Long-Term Spectroscopic and Precise Radial Velocity Monitoring of Arcturus. *Publications of the Astronomical Society of the Pacific*, **119**, 237–237. (Cited on page 14.)

Brown, K.I.T., Gray, D.F. & Baliunas, S.L. (2008). Long-Term Spectroscopic Monitoring of Arcturus. *Astrophysical Journal*, **679**, 1531–1540. (Cited on page 16.)

Carpenter, K.G. & Robinson, R.D. (1996). HST Studies of Carbon and K-M Giant/Supergiant Stars. In P. Benvenuti, F.D. Macchetto & E.J. Schreier, eds., *Science with the Hubble Space Telescope - II*, 418. (Cited on page 17.)

Carpenter, K.G., Robinson, R.D., Harper, G.M., Bennett, P.D., Brown, A. & Mullan, D.J. (1999). GHRS Observations of Cool, Low-Gravity Stars. V. The Outer Atmosphere and Wind of the Nearby K Supergiant lambda Velorum. *Astrophysical Journal*, **521**, 382–406. (Cited on page 13.)

Chapman, R.D. (1981). The 1979-1980 eclipse of Zeta Aurigae. I - The circumstellar envelope. *Astrophysical Journal*, **248**, 1043–1052. (Cited on page 13.)

Chiavassa, A., Haubois, X., Young, J.S., Plez, B., Josselin, E., Perrin, G. & Freytag, B. (2010). Radiative hydrodynamics simulations of red supergiant stars. II. Simulations of convection on Betelgeuse match interferometric observations. *Astronomy & Astrophysics*, **515**, A12. (Cited on page 5.)

Crowley, C., Espey, B.R. & McCandliss, S.R. (2008). EG And: Far Ultraviolet Spectroscopic Explorer and Hubble Space Telescope STIS Monitoring of an Eclipsing Symbiotic Binary. *Astrophysical Journal*, **675**, 711–722. (Cited on page 13.)

Decin, L., Vandenbussche, B., Waelkens, C., Decin, G., Eriksson, K., Gustafsson, B., Plez, B. & Sauval, A.J. (2003). ISO-SWS calibration and the accurate modelling of cool-star atmospheres. IV. G9 to M2 stars. *Astronomy & Astrophysics*, **400**, 709–727. (Cited on pages 15 and 17.)

Decin, L., Cox, N.L.J., Royer, P., Van Marle, A.J., Vandenbussche, B., Ladjal, D., Kerschbaum, F., Ottensamer, R., Barlow, M.J., Blommaert, J.A.D.L., Gomez, H.L., Groenewegen, M.A.T., Lim, T., Swinyard, B.M., Waelkens, C. & Tielens, A.G.G.M. (2012). The enigmatic nature of the circumstellar envelope and bow shock surrounding Betelgeuse as revealed by Herschel. I. Evidence of clumps, multiple arcs, and a linear bar-like structure. *Astronomy & Astrophysics*, **548**, A113. (Cited on page 6.)

di Benedetto, G.P. (1993). Empirical effective temperatures and angular diameters of stars cooler than the sun. *Astronomy & Astrophysics*, **270**, 315–334. (Cited on pages 14 and 15.)

Drake, S.A. (1985). Modeling lines formed in the expanding chromospheres of red giants. In J.E. Beckman & L. Crivellari, eds., *Progress in stellar spectral line formation theory; Proceedings of the Advanced Research Workshop, Trieste, Italy, September 4-7, 1984 (A86-37976 17-90). Dordrecht, D. Reidel Publishing Co., 1985, p. 351-357.*, 351–357. (Cited on pages 15, 16 and 33.)

Dupree, A.K., Lobel, A., Young, P.R., Ake, T.B., Linsky, J.L. & Redfield, S. (2005). A Far-Ultraviolet Spectroscopic Survey of Luminous Cool Stars. *Astrophysical Journal*, **622**, 629–652. (Cited on page 18.)

Dziembowski, W.A., Gough, D.O., Houdek, G. & Sienkiewicz, R. (2001). Oscillations of α UMa and other red giants. *Monthly Notices of the Royal Astronomical Society*, **328**, 601–610. (Cited on page 14.)

Eaton, J.A. (2008). A Model for the Chromosphere/Wind of 31 Cygni and Its Implications for Single Stars. *Astronomical Journal*, **136**, 1964–1979. (Cited on page 13.)

Eggen, O.J. (1971). The Arcturus Group. *Publications of the Astronomical Society of the Pacific*, **83**, 271. (Cited on page 14.)

Eggen, O.J. (1996). Star Streams and Galactic Structure. *Astronomical Journal*, **112**, 1595. (Cited on page 14.)

Gilliland, R.L. & Dupree, A.K. (1996). First Image of the Surface of a Star with the Hubble Space Telescope. *Astrophysical Journal Letters*, **463**, L29. (Cited on page 4.)

Gray, R.O., Corbally, C.J., Garrison, R.F., McFadden, M.T., Bubar, E.J., McGahee, C.E., O'Donoghue, A.A. & Knox, E.R. (2006). Contributions to the Nearby Stars (NStars) Project: Spectroscopy of Stars Earlier than M0 within 40 pc-The Southern Sample. *Astronomical Journal*, **132**, 161–170. (Cited on page 15.)

Griffin, R.E.M. (1996). Arcturus and human evolution. *The Observatory*, **116**, 404–405. (Cited on page 14.)

Harper, G.M. (2010). Betelgeuse: A Case Study of an Inhomogeneous Extended Atmosphere. In C. Leitherer, P.D. Bennett, P.W. Morris & J.T. Van Loon, eds., *Hot and Cool: Bridging Gaps in Massive Star Evolution*, vol. 425 of *Astronomical Society of the Pacific Conference Series*, 152. (Cited on page 5.)

Harper, G.M., Brown, A. & Lim, J. (2001). A Spatially Resolved, Semiempirical Model for the Extended Atmosphere of α Orionis (M2 Iab). *Astrophysical Journal*, **551**, 1073–1098. (Cited on pages 2, 3 and 4.)

Harper, G.M., Brown, A., Bennett, P.D., Baade, R., Walder, R. & Hummel, C.A. (2005). VLA Observations of ζ Aurigae: Confirmation of the Slow Acceleration Wind Density Structure. *Astronomical Journal*, **129**, 1018–1034. (Cited on page 13.)

Harper, G.M., Brown, A. & Guinan, E.F. (2008). A New VLA-Hipparcos Distance to Betelgeuse and its Implications. *Astronomical Journal*, **135**, 1430–1440. (Cited on pages 2 and 3.)

Harper, G.M., Richter, M.J., Ryde, N., Brown, A., Brown, J., Greathouse, T.K. & Strong, S. (2009). Texes Observations of M Supergiants: Dynamics and Thermodynamics of Wind Acceleration. *Astrophysical Journal*, **701**, 1464–1483. (Cited on page 4.)

Harper, G.M., O'Riain, N. & Ayres, T.R. (2013). Chromospheric thermal continuum millimetre emission from non-dusty K and M red giants. *Monthly Notices of the Royal Astronomical Society*, **428**, 2064–2073. (Cited on page 13.)

Harris, M.J. & Lambert, D.L. (1984). Oxygen isotopes in the atmospheres of Betelgeuse and Antares. *Astrophysical Journal*, **281**, 739–745. (Cited on page 3.)

Hartmann, L. & Avrett, E.H. (1984). On the extended chromosphere of Alpha Orionis. *Astrophysical Journal*, **284**, 238–249. (Cited on page 4.)

Hatzes, A.P. & Cochran, W.D. (1993). Long-period radial velocity variations in three K giants. *Astrophysical Journal*, **413**, 339–348. (Cited on pages 14, 15 and 17.)

Hatzes, A.P. & Cochran, W.D. (1998). On the nature of the radial velocity variability of Aldebaran - A search for spectral line bisector variations. *Monthly Notices of the Royal Astronomical Society*, **293**, 469. (Cited on page 17.)

Haubois, X., Perrin, G., Lacour, S., Verhoelst, T., Meimon, S., Mugnier, L., Thiébaut, E., Berger, J.P., Ridgway, S.T., Monnier, J.D., Millan-Gabet, R. & Traub, W. (2009). Imaging the spotty surface of ¡ASTROBJ¿Betelgeuse¡/ASTROBJ¿ in the H band. *Astronomy & Astrophysics*, **508**, 923–932. (Cited on pages 2, 3 and 5.)

Hoogerwerf, R., de Bruijne, J.H.J. & de Zeeuw, P.T. (2000). The Origin of Runaway Stars. *Astrophysical Journal Letters*, **544**, L133–L136. (Cited on page 2.)

Kallinger, T., Weiss, W.W., Barban, C., Baudin, F., Cameron, C., Carrier, F., De Ridder, J., Goupil, M.J., Gruberbauer, M., Hatzes, A., Hekker, S., Samadi, R. & Deleuil, M. (2010). Oscillating red giants in the CoRoT exofield: asteroseismic mass and radius determination. *Astronomy & Astrophysics*, **509**, A77. (Cited on pages 14 and 15.)

Kamiński, T., Gottlieb, C.A., Schmidt, M.R., Patel, N.A., Young, K.H., Menten, K.M., Brünken, S., Müller, H.S.P., Winters, J.M. & McCarthy, M.C. (2013). Dust-forming molecules in VY Canis Majoris (and Betelgeuse). In *EAS Publications Series*, vol. 60 of *EAS Publications Series*, 191–198. (Cited on page 4.)

Kelch, W.L., Chang, S.H., Furenlid, I., Linsky, J.L., Basri, G.S., Chiu, H.Y. & Maran, S.P. (1978). Stellar model chromospheres. VII - Capella /G5 III +/, Pollux /K0 III/, and Aldebaran /K5 III/. *Astrophysical Journal*, **220**, 962–979. (Cited on pages 17 and 18.)

Kervella, P., Verhoelst, T., Ridgway, S.T., Perrin, G., Lacour, S., Cami, J. & Haubois, X. (2009). The close circumstellar environment of Betelgeuse. Adaptive optics spectro-imaging in the near-IR with VLT/NACO. *Astronomy & Astrophysics*, **504**, 115–125. (Cited on page 5.)

Kervella, P., Perrin, G., Chiavassa, A., Ridgway, S.T., Cami, J., Haubois, X. & Verhoelst, T. (2011). The close circumstellar environment of Betelgeuse. II. Diffraction-limited spectro-imaging from 7.76 to 19.50 μm with VLT/VISIR. *Astronomy & Astrophysics*, **531**, A117. (Cited on page 5.)

Lacour, S., Meimon, S., Thiébaut, E., Perrin, G., Verhoelst, T., Pedretti, E., Schuller, P.A., Mugnier, L., Monnier, J., Berger, J.P., Haubois, X., Poncelet, A., Le Besnerais, G., Eriksson, K., Millan-Gabet, R., Ragland, S., Lacasse, M. & Traub, W. (2008). The limb-darkened Arcturus: imaging with the IOTA/IONIC interferometer. *Astronomy & Astrophysics*, **485**, 561–570. (Cited on page 14.)

Lambert, D.L., Brown, J.A., Hinkle, K.H. & Johnson, H.R. (1984). Carbon, nitrogen, and oxygen abundances in Betelgeuse. *Astrophysical Journal*, **284**, 223–237. (Cited on page 3.)

Lebzelter, T., Heiter, U., Abia, C., Eriksson, K., Ireland, M., Neilson, H., Nowotny, W., Maldonado, J., Merle, T., Peterson, R., Plez, B., Short, C.I., Wahlgren, G.M., Worley, C., Aringer, B., Bladh, S., de Laverny, P., Goswami, A., Mora, A., Norris, R.P., Recio-Blanco, A., Scholz, M., Thévenin, F., Tsuji,

T., Kordopatis, G., Montesinos, B. & Wing, R.F. (2012). Comparative modelling of the spectra of cool giants. *Astronomy & Astrophysics*, **547**, A108. (Cited on page 15.)

Levesque, E.M., Massey, P., Olsen, K.A.G., Plez, B., Josselin, E., Maeder, A. & Meynet, G. (2005). The Effective Temperature Scale of Galactic Red Supergiants: Cool, but Not As Cool As We Thought. *Astrophysical Journal*, **628**, 973–985. (Cited on page 3.)

Lim, J., Carilli, C.L., White, S.M., Beasley, A.J. & Marson, R.G. (1998). Large convection cells as the source of Betelgeuse's extended atmosphere. *Nature*, **392**, 575–577. (Cited on pages 3, 4, 5 and 28.)

Linsky, J.L. & Haisch, B.M. (1979). Outer atmospheres of cool stars. I - The sharp division into solar-type and non-solar-type stars. *Astrophysical Journal Letters*, **229**, L27–L32. (Cited on pages 16 and 17.)

Massarotti, A., Latham, D.W., Stefanik, R.P. & Fogel, J. (2008). Rotational and Radial Velocities for a Sample of 761 HIPPARCOS Giants and the Role of Binarity. *Astronomical Journal*, **135**, 209–231. (Cited on page 15.)

McClintock, W., Moos, H.W., Henry, R.C., Linsky, J.L. & Barker, E.S. (1978). Ultraviolet observations of cool stars. VI - L alpha and MG II emission line profiles (and a search for flux variability) in Arcturus. *Astrophysical Journal Supplemental Series*, **37**, 223–233. (Cited on page 33.)

McMurry, A.D. (1999). The outer atmosphere of Tau - I. A new chromospheric model. *Monthly Notices of the Royal Astronomical Society*, **302**, 37–47. (Cited on page 15.)

Merline, W.J. (1999). Precise Velocity Observation of K-Giants: Evidence for Solar-Like Oscillations in Arcturus. In J.B. Hearnshaw & C.D. Scarfe, eds., *IAU Colloq. 170: Precise Stellar Radial Velocities*, vol. 185 of *Astronomical Society of the Pacific Conference Series*, 187. (Cited on page 14.)

Meynet, G. & Maeder, A. (2003). Stellar evolution with rotation. X. Wolf-Rayet star populations at solar metallicity. *Astronomy & Astrophysics*, **404**, 975–990. (Cited on pages 2 and 3.)

Navarro, J.F., Helmi, A. & Freeman, K.C. (2004). The Extragalactic Origin of the Arcturus Group. *Astrophysical Journal Letters*, **601**, L43–L46. (Cited on page 14.)

Newell, R.T. & Hjellming, R.M. (1982). Radio emission from the extended chromosphere of Alpha Orionis. *Astrophysical Journal Letters*, **263**, L85–L87. (Cited on page 4.)

Perrin, G., Ridgway, S.T., Coudé du Foresto, V., Mennesson, B., Traub, W.A. & Lacasse, M.G. (2004). Interferometric observations of the supergiant stars α Orionis and α Herculis with FLUOR at IOTA. *Astronomy & Astrophysics*, **418**, 675–685. (Cited on page 3.)

Perrin, G., Verhoelst, T., Ridgway, S.T., Cami, J., Nguyen, Q.N., Chesneau, O., Lopez, B., Leinert, C. & Richichi, A. (2007). The molecular and dusty composition of Betelgeuse's inner circumstellar environment. *Astronomy & Astrophysics*, **474**, 599–608. (Cited on page 4.)

Perryman, M.A.C., Lindegren, L., Kovalevsky, J., Hoeg, E., Bastian, U., Bernacca, P.L., Crézé, M., Donati, F., Grenon, M., Grewing, M., van Leeuwen, F., van der Marel, H., Mignard, F., Murray, C.A., Le Poole, R.S., Schrijver, H., Turon, C., Arenou, F., Froeschlé, M. & Petersen, C.S. (1997). The HIPPARCOS Catalogue. *Astronomy & Astrophysics*, **323**, L49–L52. (Cited on pages 3, 14 and 15.)

Ramírez, I. & Allende Prieto, C. (2011). Fundamental Parameters and Chemical Composition of Arcturus. *Astrophysical Journal*, **743**, 135. (Cited on pages 14 and 15.)

Ramírez, S.V., Sellgren, K., Carr, J.S., Balachandran, S.C., Blum, R., Terndrup, D.M. & Steed, A. (2000). Stellar Iron Abundances at the Galactic Center. *Astrophysical Journal*, **537**, 205–220. (Cited on page 3.)

Retter, A., Bedding, T.R., Buzasi, D.L., Kjeldsen, H. & Kiss, L.L. (2003). Oscillations in Arcturus from WIRE Photometry. *Astrophysical Journal Letters*, **591**, L151–L154. (Cited on page 14.)

Richards, A.M.S., Davis, R.J., Decin, L., Etoka, S., Harper, G.M., Lim, J.J., Garrington, S.T., Gray, M.D., McDonald, I., O'Gorman, E. & Wittkowski, M. (2013). e-MERLIN resolves Betelgeuse at λ 5 cm: hotspots at 5 R. *Monthly Notices of the Royal Astronomical Society*, **432**, L61. (Cited on page 28.)

Richichi, A. & Roccatagliata, V. (2005). Aldebaran's angular diameter: How well do we know it? *Astronomy & Astrophysics*, **433**, 305–312. (Cited on page 15.)

Robinson, R.D., Carpenter, K.G. & Brown, A. (1998). Goddard High-Resolution Spectrograph Observations of Cool Low-Gravity Stars. IV. A Comparison of the K5 III Stars alpha Tauri and gamma Draconis. *Astrophysical Journal*, **503**, 396. (Cited on pages 15 and 17.)

Rodgers, B. & Glassgold, A.E. (1991). The temperature of the circumstellar envelope of Alpha Orionis. *Astrophysical Journal*, **382**, 606–616. (Cited on page 3.)

Ryde, N., Lambert, D.L., Richter, M.J. & Lacy, J.H. (2002). Detection of Water Vapor in the Photosphere of Arcturus. *Astrophysical Journal*, **580**, 447–458. (Cited on page 16.)

Schwarzschild, M. (1975). On the scale of photospheric convection in red giants and supergiants. *Astrophysical Journal*, **195**, 137–144. (Cited on page 2.)

Sennhauser, C. & Berdyugina, S.V. (2011). First detection of a weak magnetic field on the giant Arcturus: remnants of a solar dynamo? *Astronomy & Astrophysics*, **529**, A100. (Cited on pages 15 and 16.)

Shang, H., Glassgold, A.E., Shu, F.H. & Lizano, S. (2002). Heating and Ionization of X-Winds. *Astrophysical Journal*, **564**, 853–876. (Cited on page 37.)

Skinner, C.J., Dougherty, S.M., Meixner, M., Bode, M.F., Davis, R.J., Drake, S.A., Arens, J.F. & Jernigan, J.G. (1997). Circumstellar environments - V. The asymmetric chromosphere and dust shell of alpha Orionis. *Monthly Notices of the Royal Astronomical Society*, **288**, 295–306. (Cited on page 4.)

Soderhjelm, S. & Mignard, F. (1998). Arcturus as a double star. *The Observatory*, **118**, 365–366. (Cited on page 14.)

Tatebe, K., Chandler, A.A., Wishnow, E.H., Hale, D.D.S. & Townes, C.H. (2007). The Nonspherical Shape of Betelgeuse in the Mid-Infrared. *Astrophysical Journal Letters*, **670**, L21–L24. (Cited on page 4.)

Tsuji, T. (2000). Water on the Early M Supergiant Stars α Orionis and μ Cephei. *Astrophysical Journal*, **538**, 801–807. (Cited on page 4.)

Tsuji, T. (2008). Cool luminous stars: the hybrid nature of their infrared spectra. *Astronomy & Astrophysics*, **489**, 1271–1289. (Cited on page 17.)

Tsuji, T. (2009). The K giant star Arcturus: the hybrid nature of its infrared spectrum. *Astronomy & Astrophysics*, **504**, 543–559. (Cited on page 16.)

Turner, N.H., ten Brummelaar, T.A. & Mason, B.D. (1999). Adaptive Optics Observations of Arcturus using the Mount Wilson 100 Inch Telescope. *Publications of the Astronomical Society of the Pacific*, **111**, 556–558. (Cited on page 14.)

Uitenbroek, H., Dupree, A.K. & Gilliland, R.L. (1998). Spatially Resolved Hubble Space Telescope Spectra of the Chromosphere of alpha Orionis. *Astronomical Journal*, **116**, 2501–2512. (Cited on pages 2 and 3.)

van Leeuwen, F. (2007). Validation of the new Hipparcos reduction. *Astronomy & Astrophysics*, **474**, 653–664. (Cited on pages 2, 3 and 15.)

Verhoelst, T., Decin, L., van Malderen, R., Hony, S., Cami, J., Eriksson, K., Perrin, G., Deroo, P., Vandenbussche, B. & Waters, L.B.F.M. (2006). Amorphous alumina in the extended atmosphere of α Orionis. *Astronomy & Astrophysics*, **447**, 311–324. (Cited on page 4.)

Vögler, A. & Schüssler, M. (2007). A solar surface dynamo. *Astronomy & Astrophysics*, **465**, L43–L46. (Cited on page 2.)

Wei, L., Woody, D., Teuben, P., La Vigne, M. & Vogel, S. (2008). Bandpass Calibration for CARMA. In *CARMA Memorandum Series*, vol. 45 of *BIMA memos*. (Cited on page 9.)

Wiedemann, G., Ayres, T.R., Jennings, D.E. & Saar, S.H. (1994). Carbon Monoxide Fundamental Bands in Late-Type Stars. III. Chromosphere or CO-mosphere? *Astrophysical Journal*, **423**, 806. (Cited on pages 16 and 18.)

Williams, M.E.K., Freeman, K.C., Helmi, A. & RAVE Collaboration (2009). The Arcturus Moving Group: Its Place in the Galaxy. In J. Andersen, Nordströara, B. m & J. Bland-Hawthorn, eds., *IAU Symposium*, vol. 254 of *IAU Symposium*, 139–144. (Cited on page 14.)

Woitke, P. (2006). Too little radiation pressure on dust in the winds of oxygen-rich AGB stars. *Astronomy & Astrophysics*, **460**, L9–L12. (Cited on page 4.)

Wood, B.E., Harper, G.M., Müller, H.R., Heerikhuisen, J. & Zank, G.P. (2007). The Wind-ISM Interaction of α Tauri. *Astrophysical Journal*, **655**, 946–957. (Cited on page 18.)

Wright, K.O. (1970). The Zeta Aurigae stars. *Vistas in Astronomy*, **12**, 147–182. (Cited on page 13.)

Wright, M.C.H. (1999). Image Fidelity. In *BIMA memo 73: Image Fidelity*, vol. 73 of *BIMA memos*. (Cited on page 6.)